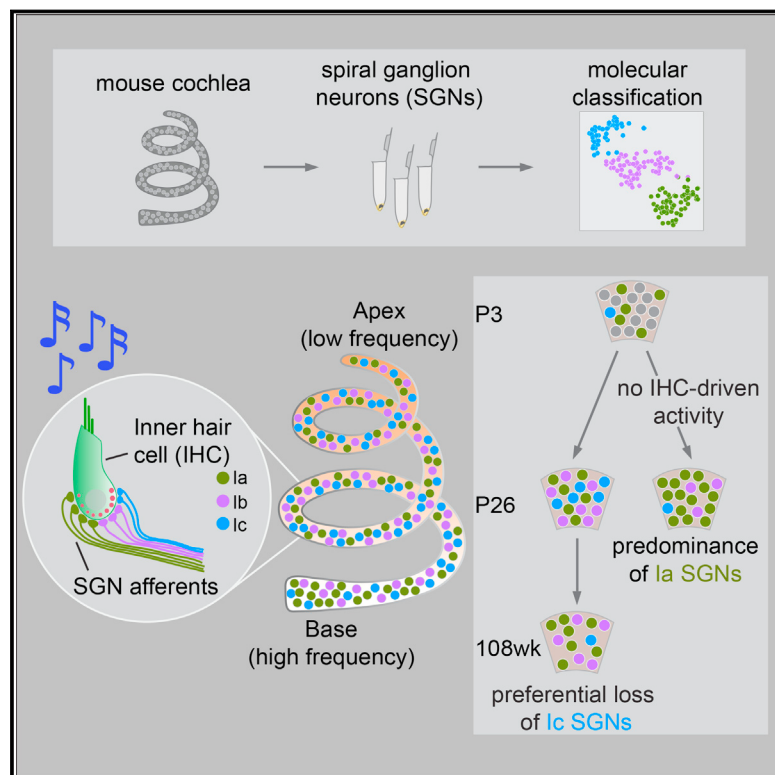


# Sensory Neuron Diversity in the Inner Ear Is Shaped by Activity

## Graphical Abstract



## Authors

Brikha R. Shrestha, Chester Chia,  
Lorna Wu, Sharon G. Kujawa,  
M. Charles Liberman, Lisa V. Goodrich

## Correspondence

[lisa\\_goodrich@hms.harvard.edu](mailto:lisa_goodrich@hms.harvard.edu)

## In Brief

Using single-cell RNA sequencing, Shrestha and colleagues define three subtypes of inner ear neurons with differential expression of physiologically relevant molecules across subtypes and tonotopically. SGN diversification begins postnatally and requires IHC-driven activity, with implications for age-related and congenital deafness.

## Highlights

- Three molecular subtypes of type I spiral ganglion neurons (SGNs) identified
- Additional molecular variations exist across subtypes and along the tonotopic axis
- Subtype identities emerge around birth and are refined over postnatal stages
- Disruption of hair-cell-driven activity leads to aberrant SGN subtype diversity

# Sensory Neuron Diversity in the Inner Ear Is Shaped by Activity

Brikha R. Shrestha,<sup>1</sup> Chester Chia,<sup>1</sup> Lorna Wu,<sup>1</sup> Sharon G. Kujawa,<sup>2,3</sup> M. Charles Liberman,<sup>2,3</sup> and Lisa V. Goodrich<sup>1,4,\*</sup>

<sup>1</sup>Department of Neurobiology, Harvard Medical School, Boston, MA 02115, USA

<sup>2</sup>Department of Otolaryngology, Harvard Medical School, Boston, MA 02115, USA

<sup>3</sup>Eaton-Peabody Laboratories, Massachusetts Eye & Ear Infirmary, Boston, MA 02114, USA

<sup>4</sup>Lead Contact

\*Correspondence: [lisa\\_goodrich@hms.harvard.edu](mailto:lisa_goodrich@hms.harvard.edu)

<https://doi.org/10.1016/j.cell.2018.07.007>

## SUMMARY

In the auditory system, type I spiral ganglion neurons (SGNs) convey complex acoustic information from inner hair cells (IHCs) to the brainstem. Although SGNs exhibit variation in physiological and anatomical properties, it is unclear which features are endogenous and which reflect input from synaptic partners. Using single-cell RNA sequencing, we derived a molecular classification of mouse type I SGNs comprising three subtypes that express unique combinations of  $\text{Ca}^{2+}$  binding proteins, ion channel regulators, guidance molecules, and transcription factors. Based on connectivity and susceptibility to age-related loss, these subtypes correspond to those defined physiologically. Additional intrinsic differences among subtypes and across the tonotopic axis highlight an unexpectedly active role for SGNs in auditory processing. SGN identities emerge postnatally and are disrupted in a mouse model of deafness that lacks IHC-driven activity. These results elucidate the range, nature, and origins of SGN diversity, with implications for treatment of congenital deafness.

## INTRODUCTION

Heterogeneity is a hallmark of the nervous system, with distinct types of neurons forming networks that subserve specific functions. Defining their cellular components is a necessary step toward understanding such networks. Across circuits with clearly different functional outputs, assignment of cell identity is relatively straightforward. For instance, in the somatosensory system, neurons that encode pain and light touch are readily distinguished by the identities of their peripheral end organs and morphologies of their endings (Abraira and Ginty, 2013). However, classification of neurons that share the same position in a circuit, perform similar function, and underlie a single modality can be challenging. For instance, the primary sensory neurons of the auditory system, the type I spiral ganglion neurons (SGNs), are all bipolar and make connections with the same sensory cell type, consistent with their shared ability to encode

sound. Their key differences are physiological, which could be imposed by other cells in the circuit. Whether type I SGNs also exhibit endogenous differences that might contribute to auditory function has remained elusive.

Type I SGNs differ in sensitivity to sound and spontaneous firing rate (SR), as revealed over 50 years ago via single-fiber recordings in the cat auditory nerve (Kiang et al., 1965). Based on the relation between threshold and SR, they were classified into three groups: low SR, medium SR, and high SR (Liberman, 1978). These three subtypes are present irrespective of tonotopic position in all vertebrate model organisms examined to date (el Barbary, 1991; Borg et al., 1988; Schmiedt, 1989; Taberner and Liberman, 2005; Winter et al., 1990). SGNs with different SRs form synapses at different positions along the basolateral surface of inner hair cells (IHCs) (Liberman, 1982) and project to different cell types in the brainstem. Such diversity enables the wide dynamic range of sound intensities encoded in the cochlea and helps maintain hearing in noisy environments (Costalupes et al., 1984; Liberman, 2017; Winter et al., 1990). In addition, immature SGNs display different firing properties in the base versus apex of the cochlea, which encode high and low sound frequencies, respectively (Mann and Kelley, 2011). Whether mature SGNs retain these differences and how they vary among SR subtypes are not known.

Because type I SGNs have been classified physiologically, the nature and origin of their underlying heterogeneity are unclear. At one extreme, there may be one basic type of SGN that exhibits different firing properties because of the input received from its pre-synaptic partners. Both heterogeneity in presynaptic vesicle release probability in IHCs (Frank et al., 2009) and regulation by olivocochlear efferents (Guinan, 2018; Liberman, 1980) have been suggested to contribute to SGN physiological diversity. Alternatively, SGNs may express different collections of receptors and ion channel regulators that shape their sensitivity and SR. Indeed, hints of molecular heterogeneity have been noted (Adamson et al., 2002; Chen et al., 2011; Liu and Davis, 2014; Liu et al., 2014), although it was not possible to link any one marker with known electrophysiological signatures. Without a comprehensive understanding of SGN molecular profiles, the ways SGNs actively influence auditory coding remain to be defined.

The lack of knowledge of subtype-specific molecular signatures represents a major barrier in understanding SGN biology and function, with direct implications for human health.

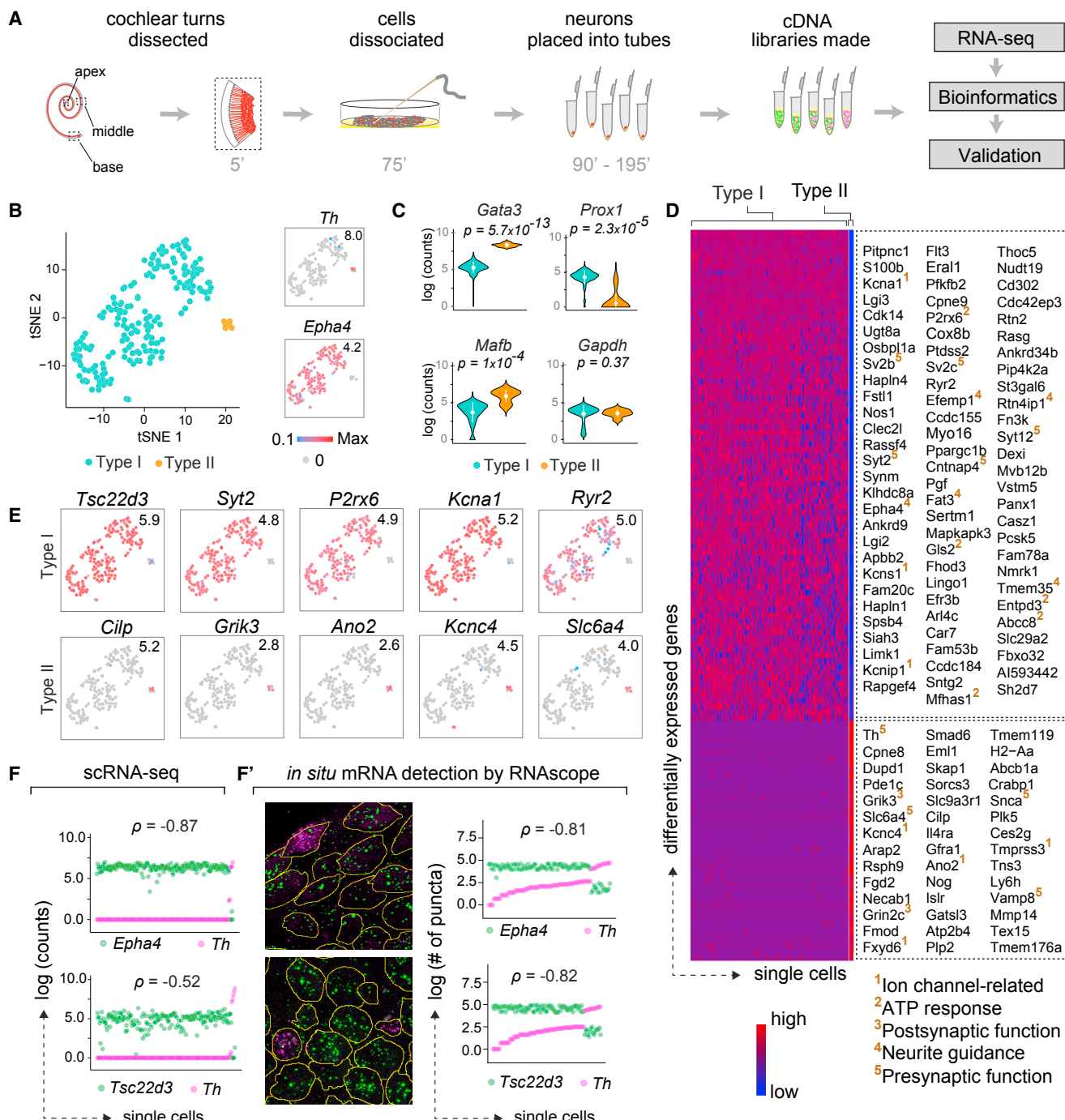


**Figure 1. Type I and II SGNs Can Be Detected as Molecularly Distinct Cell Populations Using scRNA-Seq**

(A) Workflow for single-cell RNA-seq (scRNA-seq) of spiral ganglion neurons (SGNs). Numbers indicate time elapsed (in minutes) since animal euthanization. (B) t-stochastic neighbor embedding (t-SNE) of neuronal profiles ( $n = 186$ , 11 P25–P27 animals) revealed several clusters. Clusters of types I (blue) and II (orange) SGNs were identified by expression of *EphA4* and *Th*, respectively (insets). In this and all subsequent t-SNE plots, numbers in the upper right corner indicate highest expression (Max) observed for each gene.

(C) Violin plots comparing gene expression among types I and II SGNs illustrate increased expression of *Gata3* and *Mafb* in type II SGNs ( $p = 5.7 \times 10^{-13}$  and  $1 \times 10^{-4}$ , respectively), and of *Prox1* in type I SGNs ( $p = 2.3 \times 10^{-5}$ ), with no difference in the expression of the housekeeping gene *Gapdh* ( $p = 0.37$ ). The white dots and the error bars indicate the mean and the SD, respectively.

(D) Heatmap showing genes expressed differentially between types I and II SGNs, with examples of type-I-enriched (top panel) and type-II-enriched (bottom panel) genes listed on the right. Superscript numbers indicate gene functional groups annotated manually.

(legend continued on next page)

Low-SR SGNs are lost after noise damage (Furman et al., 2013) and as a consequence of aging (Schmiedt et al., 1996), which may explain the difficulties understanding speech amid background noise in older individuals. However, in the absence of subtype-specific molecular tools, efforts to assign functions to individual subtypes and to understand the mechanisms underlying selective vulnerability have been limited. Similarly, since SGN subtypes do not exhibit mature physiological properties until the end of the first month in mice (Liberman and Liberman, 2016), the factors that give rise to their diverse properties during development remain elusive, despite the potential for SGN pathology in congenital deafness.

Single cell transcriptome-based approaches offer a powerful way to investigate heterogeneity in neuronal populations. To characterize neuronal diversity in the cochlea, we generated high-resolution transcriptomic profiles of individual SGNs. We found three molecularly distinct subtypes (Ia, Ib, and Ic) that match the anatomical features of high-, medium-, and low-SR SGNs, with additional variation along the tonotopic axis. SGN identities emerge gradually in development and this diversification requires IHC-driven activity. This comprehensive view of SGN heterogeneity uncovers endogenous differences that could directly affect auditory coding and highlights the importance of activity for establishing these differences during development, with important implications for the effects of age-related and congenital hearing loss on SGN composition.

## RESULTS

### Type I and Type II SGNs Exhibit Clear Molecular Differences

To survey SGN heterogeneity in an unbiased manner, we manually collected individual SGNs from the basal, middle, and apical turns of cochlea of young adult mice (P25–P27, 11 animals) and analyzed them by single-cell RNA sequencing (scRNA-seq) (Figure 1A; see the STAR Methods). A total of 186 wild-type SGN single-cell libraries passed all quality control criteria (Figure S1A). In a two-dimensional representation generated using t-stochastic neighbor embedding (t-SNE), SGN libraries segregated into several distinct groups (Figure 1B). Types I and II SGNs, which exhibit well-characterized differences in anatomy, glutamate-responsiveness, myelination, and synapse number (Berglund and Ryugo, 1987; Glowatzki and Fuchs, 2002; Spoendlin, 1979; Weisz et al., 2009), fell into distinct groups enriched for known markers, such as *Epha4* and *Th*, respectively. Presumed type I and type II SGNs also express different levels of *Gata3* ( $p = 5.7 \times 10^{-13}$ ), *Mafb* ( $p = 1 \times 10^{-4}$ ), and *Prox1* ( $p = 2.3 \times 10^{-5}$ ), as previously reported (Figure 1C) (Nishimura et al., 2017). Housekeeping genes, such as *Gapdh* ( $p = 0.37$ ) (Figure 1C) and *Eif2a* ( $p = 0.43$ ; data not shown), are expressed at comparable levels in all SGNs. Overall, types I and II SGNs compose 96% and

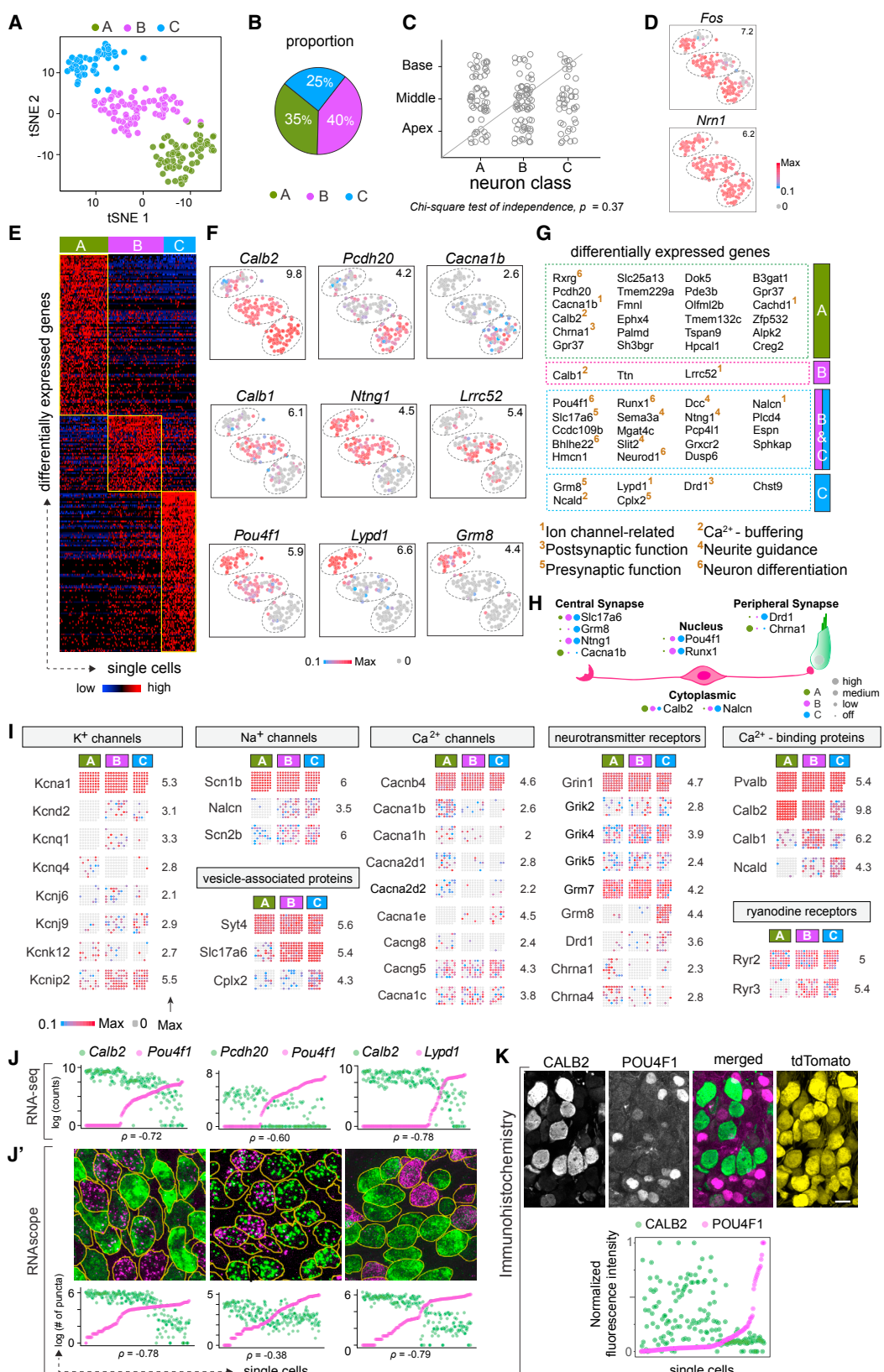
4% of the samples, respectively, which is close to histological estimates of their proportions (Spoendlin, 1969).

Types I and II SGNs exhibit profound differences in connectivity and function that predict similar distinctions at the molecular level. The myelinated type I SGNs encode all the signals we think of as “hearing” (Kiang et al., 1967; Sachs and Abbas, 1974), whereas unmyelinated type II SGNs may mediate auditory pain and nociception (Flores et al., 2015). Like other neurons representing different modalities, type I and type II SGNs exhibit broad differences at the molecular level, with >1,700 differentially expressed genes ( $p < 0.01$  or lower) (Table S1A). Of these, 335 genes show a binary ON/OFF expression between the two cell classes (defined operationally as expressed in >70% and <20% of cells for ON and OFF, respectively) (examples in Figure 1E). Gene ontology (GO) analysis of differential expression revealed overrepresentation of molecules involved in neuronal function and innervation (Figure S1J). Additional manual categorization of the top-50 genes highlighted a stark difference in the presynaptic vesicle-associated protein profiles between types I and II SGNs, with highly specific expression of *Sv2b*, *Sv2c*, *Syt2*, and *Syt12* in type I SGNs and of *Snca*, *Vamp8* in type II SGNs (Figure 1D). In addition, whereas both subtypes co-express several glutamate receptor subunits (e.g., *Grin1*, *Grin2a*, *Grin4*) (data not shown), type II SGNs show unique expression of *Grin2c* and *Grin3* (Figure 1D). Type I and type II SGNs also express different sets of potassium ( $K^+$ ) channel subunits, with *Kcn1* and *Kcnip1* in type I and *Kcn4* in type II SGNs (Figure 1D). These results suggest distinctions in glutamate responsiveness, presynaptic release properties, and neuronal excitability consistent with previous reports of different electrophysiological signatures between these SGN subtypes (Glowatzki and Fuchs, 2002; Weisz et al., 2014).

Validation using RNAscope, an *in situ* approach for semi-quantitative RNA detection (Advanced Cell Diagnostics), confirmed that the variation detected by scRNA-seq represents bona fide differences. In tissue sections of P25–P27 mouse cochleas, levels of *Th*, which mark the small type II subpopulation in our scRNA-seq data (Figure 1B, inset), were highest in cells with the lowest levels of *Epha4*, a type I marker (Figure 1F). *Tsc22d3* transcripts were detected in neurons negative for the type II marker *Th* (Figure 1F') and overlapped with expression of the type I marker *Epha4* (data not shown), indicating that it may be a reliable type I marker as predicted by scRNA-seq (Figure 1F'). Thus, our approach allowed sampling and detection of the type II subtype comprising only a small minority of SGNs (Spoendlin, 1969). Despite the small size and number of type II SGNs, an average of 6,320 genes/cell and >11,000 genes across all cells could be detected, including cell-type-specific molecules that influence neuron physiology and connectivity. These findings confirm that transcriptomic SGN profiles can be used to establish a molecular framework for subtype classification.

(E–F') t-SNE plots showing examples of genes with binary ON/OFF expression (color key shown in B) between the two subtypes (E), with clear correspondence between scRNA-seq (F) and RNAscope (F') quantification in P25–P27 tissue sections for *Epha4* and *Th*, as well as the novel type I marker *Tsc22d3*. In images showing RNAscope puncta (F'), SGN cell bodies are outlined in yellow as visualized by immunostaining for parvalbumin (data not shown). In scatterplots (F and F'), the two dots in each column indicate counts for two different genes in the same neuron, and neurons are sorted along the x axis by the level of the gene in magenta.  $p$  represents Pearson's correlation coefficient.

See also Figure S1 and Tables S1 and S2.



(legend on next page)

### Three Molecularly Defined Subtypes of Type I SGNs

Next, we focused our analysis on type I SGNs, which were identified as *EphA4<sup>+</sup> Th<sup>-</sup>* cells in the scRNA-seq libraries (Figure 1B, insets). In a t-SNE plot, type I SGNs further segregated into three distinct groups (Figure 2A). Independent classification using an unsupervised machine-learning strategy (i.e., graph-based clustering; see the STAR Methods) categorized type I SGNs into three distinct subtypes (Ia, Ib, and Ic) (Figures 2A, S1B, and S1C) that compose 35%, 40%, and 25%, respectively, of the total population (Figure 2B). Both projection of SGN transcriptomes onto principal component analysis (PCA) space (Figure S1D) and hierarchical clustering by Ward's method (Figure S1E) revealed three broad subtypes and close correspondence with the cell identities that were independently predicted by the graph-based clustering approach (Figure 2A). Thus, multiple statistical methods indicate that there are three molecularly distinct type I SGN subtypes.

This classification scheme was not influenced by experimental and biological variables. First, the clusters do not correspond to where the neurons originated in the cochlea (chi-square test,  $p = 0.37$ ) (Figures 2C, S1D, and S1E). Second, clustering is not driven by the acoustic exposure history of the animal, as activity-induced genes such as *Fos* and *Nrn1* were expressed in comparable proportions of cells (Figure 2D). Furthermore, no significant differences were found across the clusters in experimental factors such as animal identity, cDNA processing batch, sequencing batch, genes detected, or proportions of spike-in and mitochondrial transcripts (Figures S1F and S1G). Third and finally, none of the single-cell libraries were positive for glial markers (Figure S1H).

Differential expression analysis among Ia, Ib, and Ic SGNs revealed 425 genes (all at  $p < 0.01$ ) with subtype-enriched expression (Table S1B; top 100 or all for each subtype depicted in Figure 2E). The segregation into three subtypes is associated with striking differences in expression of multiple genes, including *Calb2*, *Pou4f1*, *Ntng1*, and *Lypd1*. Of these, *Calb2* and *Pou4f1* are expressed in complementary gradients: *Calb2* is highest in Ia and lowest in Ic, with *Pou4f1* highest in Ic and lowest in Ia ( $p = -0.73$ ) (Figure 2F). Ib and Ic SGNs both express high levels

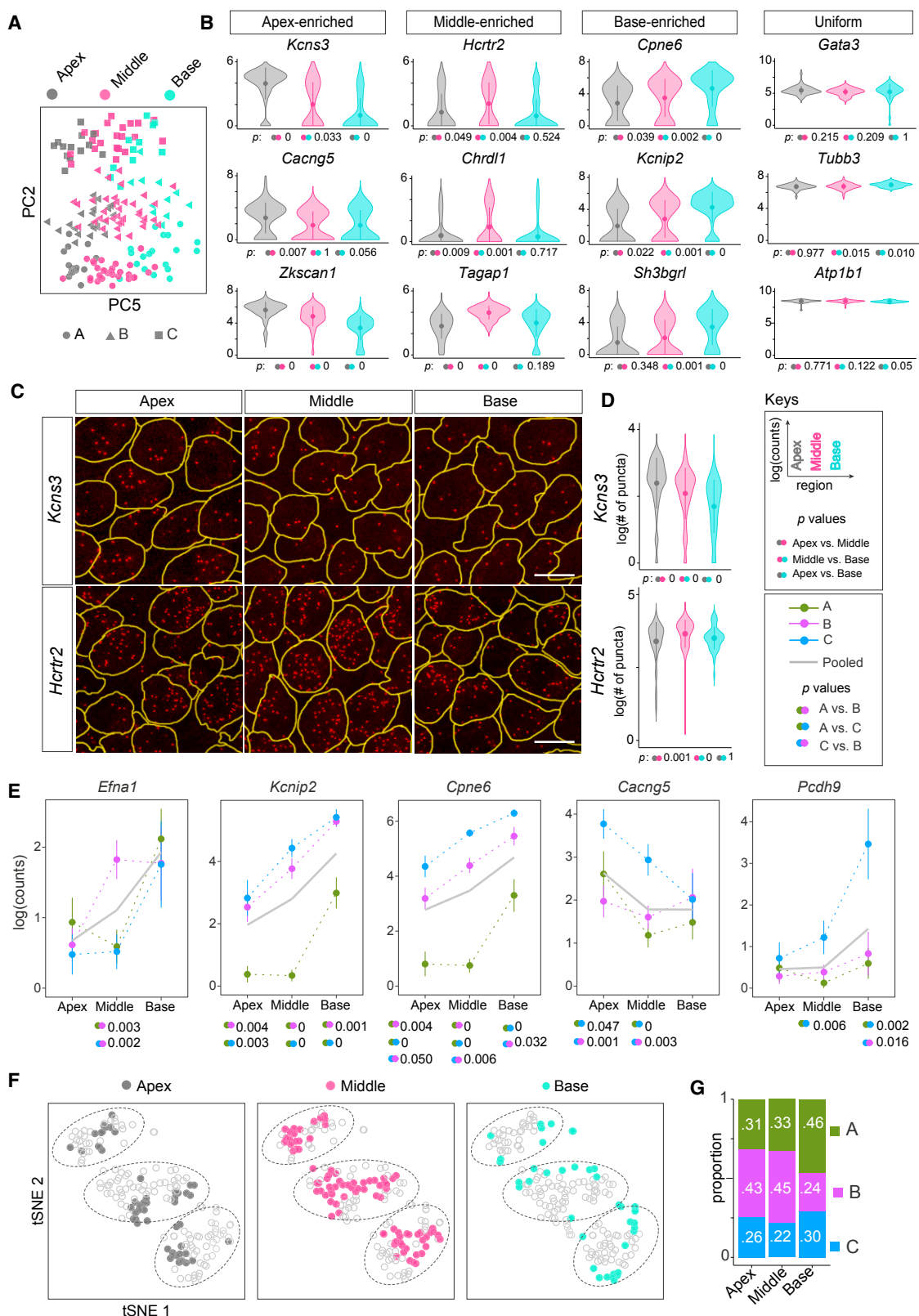
of *Ntng1*, but can be further distinguished by expression of *Lypd1*, which overlaps partially with *Pou4f1* and *Ntng1* ( $\rho = 0.71$ , 0.49, respectively), and is expressed at higher levels in Ic SGNs than in Ib SGNs (Figure 2F). *Pcdh20*, *Cacna1b*, *Lrrc52*, and *Grm8* were also expressed in subtype-specific patterns (Figure 2F). In contrast, pan-neuronal genes, such as *Tubb3*, *Gria2*, and *Atp1b1*, were expressed broadly (100%, 99%, and 99% of cells, respectively) (Figure S1I).

Genes that are expressed differentially across subtypes are mostly involved in regulating neuronal differentiation, connectivity, and physiology. In a GO analysis, “potassium channel activity,” “calcium (Ca<sup>2+</sup>) ion binding,” “signal transducer activity,” “neuron differentiation,” “regulation of ion transport,” and “axon development” were among the 54 biological processes enriched significantly ( $p < 0.01$ ) (Figure S1K). Genes encoding proteins that localize to “synapse,” “cation channel complex,” and “plasma membrane” were also overrepresented. Manual annotation revealed combinatorial expression of several transcription factors, further indicating that SGN subtypes express distinct cohorts of genes that might influence their differentiation: *Rxrg* is expressed mostly in Ia, *Runx1* is primarily in Ib and Ic, and *Pou4f1* is in a decreasing gradient from Ic to Ia. Similarly, the subtypes express unique combinations of genes encoding Ca<sup>2+</sup>-binding proteins, with *Calb2*, *Calb1* and *Ncald* enriched in Ia, Ib and Ic SGNs, respectively. Ib and Ic SGNs also show enriched expression of molecules related to neurite guidance (e.g., *Ntng1*, *Sema3a*, *Dcc*, *Slc2*) and presynaptic release (e.g., *Slc17a6*, *Cpx2*) (Figure 2G).

The molecular signatures of SGN subtypes suggest meaningful physiological differences. Several proteins related to synaptic transmission or neuronal physiology were among those differentially expressed, and a comprehensive assessment of their gene families revealed both broad and subtype-specific expression (Figures 2I, S2, and S3). Among glutamate receptors, several AMPA-type subunits (e.g., *Gria2*, *Gria3*, *Gria4*) were uniformly expressed, but *Grik4* was expressed in an increasing gradient from Ia to Ic, while the metabotropic receptor subunit *Grm8* was specifically expressed in Ic SGNs (Figures 2I and S3). Whereas the cholinergic receptor subunits *Chrna1* and *Chrna4*

### Figure 2. Three Molecular Subtypes of Type I SGNs Exist in the Mouse Inner Ear

(A and B) t-SNE embedding of type I SGN transcriptomes (A) depicting three clusters—A, B, and C—predicted by unsupervised graph-based clustering, which are indicated by dot color. Overall proportions are illustrated in (B). (C and D) SGN subtypes are present in all regions of the cochlea (C) and show expression of the activity-induced genes *Fos* and *Nrn1* in all clusters (D). (E–G) SGNs in the three clusters exhibit broad differences in their transcriptomes, illustrated in a heatmap for the top-100 differentially expressed genes (E) and in t-SNE plots for individual genes that show subtype-specific expression patterns (F). Numbers in the upper-right corner indicate the highest expression (Max) observed for each gene. Genes enriched across the three subtypes encode proteins associated with many aspects of neuronal differentiation and function (G). Superscript numbers indicate gene functional groups annotated manually. (H) Examples of differentially expressed genes that encode proteins predicted to localize to different neuronal compartments, indicating that input and output properties vary among SGNs. For each gene, expression level among SGN subtypes is schematized as the size of each colored dot. (I) Expression of select genes relevant to neuronal physiology is illustrated in dot matrix plots of individual libraries, which are grouped by subtype. Some genes are expressed uniformly across all libraries (top row for each group), whereas others vary across subtypes (all other rows). Numbers on the right indicate the highest expression (Max) observed for each gene. (J–K) Differentially expressed genes identified by scRNA-seq (J) showed the same patterns of expression in individual SGNs analyzed by RNAscope of P25–P27 tissue sections (J'). SGN cell bodies are outlined in yellow as visualized by immunostaining for parvalbumin (data not shown). Similarly, immunostaining (K) for CALB2 (calretinin) (green), POU4F1 (magenta), and tdTomato (yellow) in tissue sections of P25–P27 *bhlhb5<sup>Cre/+</sup>; Ai14/+* mice revealed inverse gradients of CALB2 and POU4F1 expression, quantified below. In scatterplots (J, J', and K), the two dots in each column indicate expression levels of two different markers in the same neuron, and neurons are sorted along the x axis by the level of the gene in magenta. Scale bars, 10 μm (K). See also Figures S1, S2, and S3 and Tables S1 and S2.



(legend on next page)

were enriched in Ia SGNs, Ic SGNs showed enriched expression of *Drd1*, which encodes a dopamine receptor subunit (Figures 2I and S3). Among genes encoding K<sup>+</sup> channel subunits, *Kcnq4* and *Kcnd2* were detected mostly in Ia and Ib, respectively, with enriched expression of *Kcnip2* and *Kcnj9* in Ib and Ic SGNs (Figures 2I and S2). The voltage-gated Ca<sup>2+</sup> channels *Cacna1b*, *Cacna1h*, and *Cacna2d1* were all enriched in Ia SGNs (Figures 2I and S2). Expression of the leak sodium (Na<sup>+</sup>) channel *Nalcn* was restricted to Ib and Ic neurons, whereas the voltage-gated Na<sup>+</sup> channel subunit *Scn2b* was expressed in a decreasing gradient from Ic to Ia (Figures 2I and S2). Taken together, these findings suggest that the three molecularly defined type I SGN subtypes constitute physiologically distinct subpopulations.

RNAscope validation confirmed that the same genes that drive SGN segregation in the scRNA-seq data can be used to identify Ia, Ib, and Ic subtypes in cochlear sections of P25–P27 mice. As seen by scRNA-seq (Figure 2J), *Calb2* and *Pou4f1* are expressed in opposing gradients among SGNs ( $p = -0.78$ ) (Figure 2J'). *Pcdh20* levels are highest in cells negative for *Pou4f1* transcripts and lower in all other cells, indicating a weak negative correlation ( $p = -0.38$ ). *Lypd1* expression is restricted to cells largely off or low for *Calb2* ( $p = -0.79$ ). Thus, these results validated both individual gene-level variation as well as gene-gene relationships across SGN populations. Furthermore, a negative correlation was observed between CALB2 and POU4F1 protein levels in SGNs ( $p = -0.36$ ) (Figure 2K), suggesting that the observed transcript-level differences may be functionally significant.

#### Tonotopic Differences

To gain further insights into type I SGN heterogeneity, we examined other sources of variation in the data revealed by PCA. We found that although differences corresponding to the Ia, Ib, and Ic subtypes can be accounted for largely by principal component 2 (PC2), additional heterogeneity represented by PC5 diversified SGNs within each subtype (Figure 3A). This orthogonal axis of heterogeneity corresponded to the tonotopic origin of the SGNs, which was recorded for every cell during dissociation and manual collection. This result motivated further analysis of differences related to tonotopy both at the single-cell and at the tissue levels.

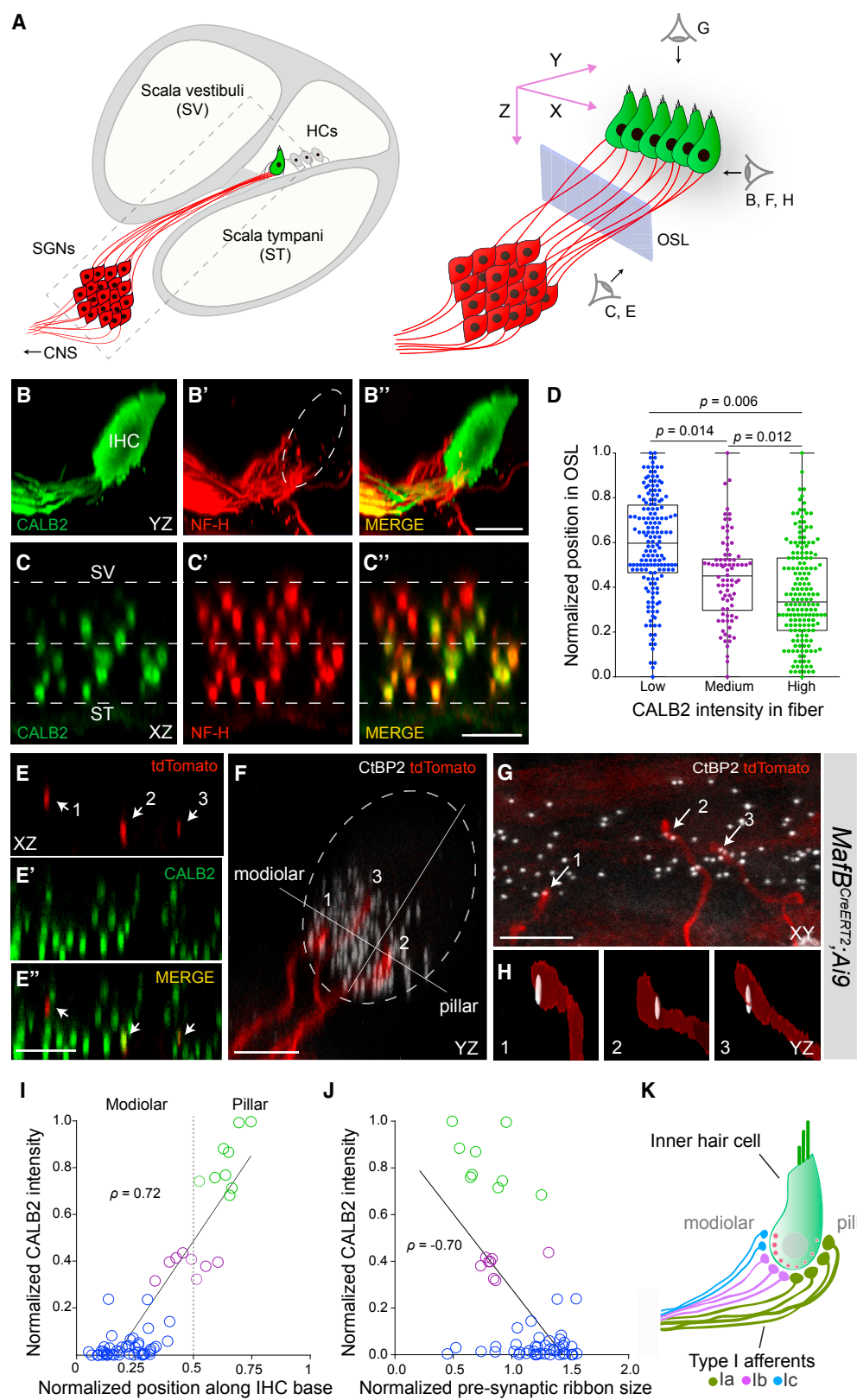
We grouped the single-cell transcriptomic profiles based on cochleotopic position instead of molecular identity and examined gene expression differences among such groups. As predicted by PCA results (Figure 3A), this analysis revealed an

additional but subtler variation, with 114 genes expressed differentially among neurons from the three cochlear regions, compared to 425 genes that differ across subtypes ( $p < 0.01$ ) (Figure S4A; Table S1C). Unlike the genes that drive the Ia, Ib, and Ic classification, region-enriched genes were expressed mostly in gradients (Figure 3B). For example, genes for two K<sup>+</sup> channel subunits (*Kcns3*, *Kcnip4*) and several guidance-related factors (*Ntng2*, *Wnt3*) were enriched in the apex (Figure S4A). RNAscope of P25–P27 mouse cochlea validated the tonotopic variation in expression observed by scRNA-seq. Levels of *Kcns3*, which encodes the Kv9.3 K<sup>+</sup> channel subunit, were highest in the apex, lower in the middle, and even lower in the base of the cochlea (median number of puncta per cell: 11.5, 9, and 6, respectively) (Figures 3C and 3D). Similarly, expression of *Hcrt2*, which encodes the hypocretin receptor type 2, was highest in the middle of the cochlea and lower in both the apex and the base (median number of puncta per cell: 44, 34, and 33, respectively) (Figures 3C and 3D), consistent with scRNA-seq results (Figure 3B). By contrast, expression of the pan-neuronal marker *Tubb3* showed minimal variation (median number of puncta per cell: 86, 85, and 89 in apex, middle, and base, respectively) (Figure S4B), indicating that the observed variability in *Kcns3* and *Hcrt2* transcripts is unlikely to be due to technical artifacts.

Closer analysis revealed that some genes vary along the tonotopic axis in a subtype-specific manner. For example, *Efna1*, which encodes the axon guidance molecule Ephrin A1, is expressed at higher levels in the middle and base relative to the apex among Ib SGNs, but only enriched in the base among Ia and Ic SGNs (Figure 3E). Both *Kcnip2* and *Cpne6* are expressed in an apical-basal ascending gradient among Ib and Ic SGNs, but selectively enriched in the base among Ia SGNs (Figure 3E). *Cacng5*, which encodes a voltage-gated Ca<sup>2+</sup> channel subunit, shows a particularly complex pattern, with an apical-basal descending gradient among Ic SGNs, an apical-middle descending gradient among Ia SGNs, and relatively uniform expression among Ib SGNs. *Pcdh9* is expressed in an apical-basal gradient but only among Ic SGNs. We did not observe subtype-specific variation in expression for known pan-neuronal genes, such as *Tubb3* and *Atp1b1*, or other weakly expressed genes that exhibit tonotopic variation, such as *Ntng2* and *Wnt3* (Figure S4C), suggesting that such differences are not artificial. Overall, analysis across the tonotopic axis for each individual class of SGNs revealed 184, 157, and 183 genes with regional differences in

#### Figure 3. Type I SGNs Exhibit both Broad and Subtype-Specific Tonotopic Differences

- (A) Molecular heterogeneity exists along the tonotopic axis of the cochlea. Projection of single-cell transcriptomes onto principal component analysis (PCA) space shows that PC2 reflects differences among the A, B, and C subtypes, whereas PC5 captures heterogeneity that corresponds to tonotopic origin.
- (B) Violin plots illustrate examples of genes that show either differential or uniform expression across the three tonotopic regions. Dunn's test was used to assess significance for each possible comparison, as indicated by colored dots next to p values. Dots and error bars represent mean and SD, respectively. See keys next to (D).
- (C and D) Regional differences in expression of *Kcns3* and *Hcrt2* were confirmed by RNAscope of P25 tissue sections (C) and quantified in (D).
- (E) Further analyses of scRNA-seq data revealed that some genes exhibit regional variation in a subtype-specific manner. Trends for all SGNs are shown in gray solid lines and for Ia (green), Ib (purple), and Ic (blue) SGNs in dashed lines. Dots and error bars represent mean and SEM, respectively. Pairs of dots indicate p values for comparisons across tonotopic regions by Tukey's honestly significant difference (HSD) test if the data were normally distributed and Dunn's test otherwise. p values are reported only for statistically significant differences. See keys next to (D).
- (F and G) SGN subtypes are present in all regions of the cochlea, as revealed by t-SNE plots showing the anatomic origin of cells (apex, middle, and base) in each cluster (F). However, the proportions differ in the basal turn of the cochlea compared to the apex and the middle (G). Scale bars, 10 μm (C).
- See also Figure S4 and Tables S1 and S2.



(legend on next page)

expression among Ia, Ib, and Ic SGNs, respectively (Tables S1D–S1F). Of the 524 total genes, 494 were unique, which is 3 times higher than the genes identified in subtype-blind comparisons. Only 77 of the 524 genes overlapped with the gene list derived from subtype-blind comparisons. Thus, a subtype-aware analysis of scRNA-seq data unmasked a new layer of tonotopic variation among SGNs.

Even some of the genes that vary among SGN subtypes exhibit additional variation along the cochlear axis. The most robust subtype markers, such as *Calb2*, *Cacna1b*, *Ntng1*, and *Lypd1*, were expressed at similar levels in the apex, middle, and base (Figure S4D). However, some functionally relevant genes (e.g., *Lrrc52*, *Kcnip4*, *Anxa5*, *Ryr3*) showed additional regional differences (Figure S4E). For instance, the potassium channel subunit *Kcnip4* was enriched in Ia SGNs in the apex and middle, but in Ic SGNs in the base. This indicated that, although the molecular identities of Ia, Ib, and Ic SGNs across the cochlea are largely similar, subtle variations exist in some regions, particularly in the base.

To further investigate how SGNs vary across the three major turns of the cochlea (apex, middle, base), we annotated the anatomic origin of every neuron in t-SNE plots that depict SGN subtypes. We observed different proportions of SGN subtypes in each turn (Figure 3F). In the middle turn, there were 33% Ia, 45% Ib, and 22% Ic SGNs. The proportions were similar in the apex (31% Ia, 43% Ib, and 26% Ic) (Figure 3G). However, the base contained a higher proportion of Ia SGNs (46%), largely at the expense of Ib SGNs (24%). Thus, tissue-level variation in SGN-subtype proportions is a tonotopic feature superimposed on gene expression gradients across the mouse cochlea.

### Types Ia, Ib, and Ic SGNs Exhibit Stereotyped Anatomical and Morphological Differences

Previous studies showed synapse size differences and spatial segregation of the peripheral projections of the three SR groups (Kawase and Liberman, 1992; Liberman, 1982; Liberman et al., 2011). To map our molecular classification onto the known anat-

omy, we took advantage of sparse labeling of SGNs in the *Mafb*<sup>CreERT2</sup>;Ai9 transgenic line to trace neuronal projections from the cell body to the peripheral synapse (Figures 4 and S5). Consistent with scRNA-seq and RNAscope results, levels of the calcium-binding protein CALB2 (calretinin) varied among SGN fibers (Figures 4B–B''). Double staining for CALB2 revealed that levels in peripheral processes correlated strongly ( $p = 0.86$ ) with those in the cell body (Figures S5A and S5B). Thus, CALB2 levels in individual fibers can be used to identify SGN molecular subtypes.

We observed a striking organization of Ia, Ib, and Ic peripheral processes coursing through the osseous spiral lamina (OSL), which is flanked by *scala vestibuli* (SV) and *scala tympani* (ST) (Figure 4A). In optical cross-sections of image stacks capturing CALB2- and neurofilament (NF)-labeled afferent processes in the OSL in the P25–P27 cochlea (Figures 4C–4C''), fibers with the highest levels of CALB2 (CALB2<sup>high</sup> NF<sup>+</sup>) were closer to ST, while those with the lowest level of CALB2 (CALB2<sup>low</sup> NF<sup>+</sup>) were closer to SV. The mid-OSL region was occupied by fibers with intermediate CALB2 levels (CALB2<sup>mid</sup> NF<sup>+</sup>) (Figure 4D). This organization matches the projections of low-, medium-, and high-SR SGNs along the SV-ST axis (Kawase and Liberman, 1992). Examination of tdTomato-labeled olivocochlear efferent axons in *Chat*<sup>Cre</sup>;Ai14 mice indicated comparatively even distribution across the OSL (Figures S5E–S5G) in contrast with tdTomato–NF<sup>+</sup> SGN processes. Thus, the presence of CALB2<sup>low</sup> NF<sup>+</sup> fibers closer to SV is not conflated by olivocochlear axon organization.

The position and morphology of synapses also matched known differences among SR subtypes. By following sparsely labeled SGN processes from the OSL to their IHC terminals ( $n = 61$  SGNs, 5 P25–P27 *Mafb*<sup>CreERT2</sup>;Ai9 animals) (Figures 4E–4H), we found that peripheral axons with low CALB2 expression (Ic subtype) ran closer to SV and could be traced to the modiolar aspect of IHCs (Figure 4I), where they formed synapses with large presynaptic ribbons (Figure 4J). Conversely, fibers with high CALB2 levels (Ia subtype) were closer to ST, projected to the pillar face (Figure 4I), and formed synapses with small ribbons

**Figure 4. Type I SGN Peripheral Processes and Synapses Are Anatomically Segregated by Subtype**

- (A) Schematic depicting a cross-section of the cochlea (left) with a magnified view of the boxed area on the right. The three perspectives corresponding to the cochlear whole-mount images in (B)–(H) are indicated (right). The blue rectangle represents the plane of section through confocal image stacks of afferent fibers (red) extending through the osseous spiral lamina (OSL) to terminate along the basolateral surface of the hair cell (HC) (green).
- (B–C'') Side (B) and cross-sectional (C) views of a whole-mount cochlea stained for CALB2 (green, B and C) and NF-H (neurofilament heavy chain) (red, B' and C''), with merged images (B'' and C''). CALB2<sup>+</sup> fibers preferentially project toward the pillar side of the inner hair cell (IHC) compared to the total population of all NF-H<sup>+</sup> SGN processes and are segregated along the *scala vestibuli* (SV)–*scala tympani* (ST) axis in the OSL (C–C''). CALB2 antibody also labels IHCs.
- (D) Afferent fiber distribution in the OSL depicted as box and whisker plots. CALB2 fluorescent intensity levels were measured for all NF-H<sup>+</sup> fibers in the OSL cross-section ( $n = 5$  animals). Fibers were split into three groups based on CALB2 levels: “low CALB2” ( $n = 165$  fibers), “medium CALB2” ( $n = 82$  fibers), and “high CALB2” ( $n = 174$  fibers). The distance from the median center of each nerve bundle was calculated for individual fibers from each cluster. Error bars represent minimum and maximum values.  $p$  values indicate the results of Tukey’s HSD test following one-way ANOVA.
- (E–H) Individual tdTomato-labeled fibers (red) (E and E'') were traced in cochlear whole mounts from *Mafb*<sup>CreERT2</sup>;Ai9 animals that were also stained for CALB2 (green, E' and E'') to assign subtype identity. Presynaptic ribbons were defined by co-staining for CtBP2 (white, F–H). In this example, three individual tdTomato-labeled SGN fibers (arrows) express “high” (2), “medium” (3), and “low” (1) levels of CALB2 as they project through the OSL (E and E''). The same three fibers segregate along the modiolar–pillar axis of the IHC, shown in side view in (F). Each tdTomato-labeled fiber terminates opposite a single presynaptic ribbon, shown in high-resolution reconstructions (H).
- (I and J) Quantification of all analyzed fibers ( $n = 61$ , 5 animals) revealed that both fiber position (I;  $p = 0.72$ ) and ribbon size (J;  $p = -0.70$ ) correlate with CALB2 intensity.
- (K) Type Ia (green), Ib (purple), and Ic (blue) SGNs extend peripheral processes that are segregated in the OSL and along the modiolar–pillar axis of the IHC, where they are apposed by presynaptic ribbons that decrease in size along the same axis. These features match those described for high-, medium-, and low-SR SGNs. Scale bars, 10 (B'', C'', E'', and F) and 5  $\mu\text{m}$  (G).
- See also Figure S5 and Table S2.

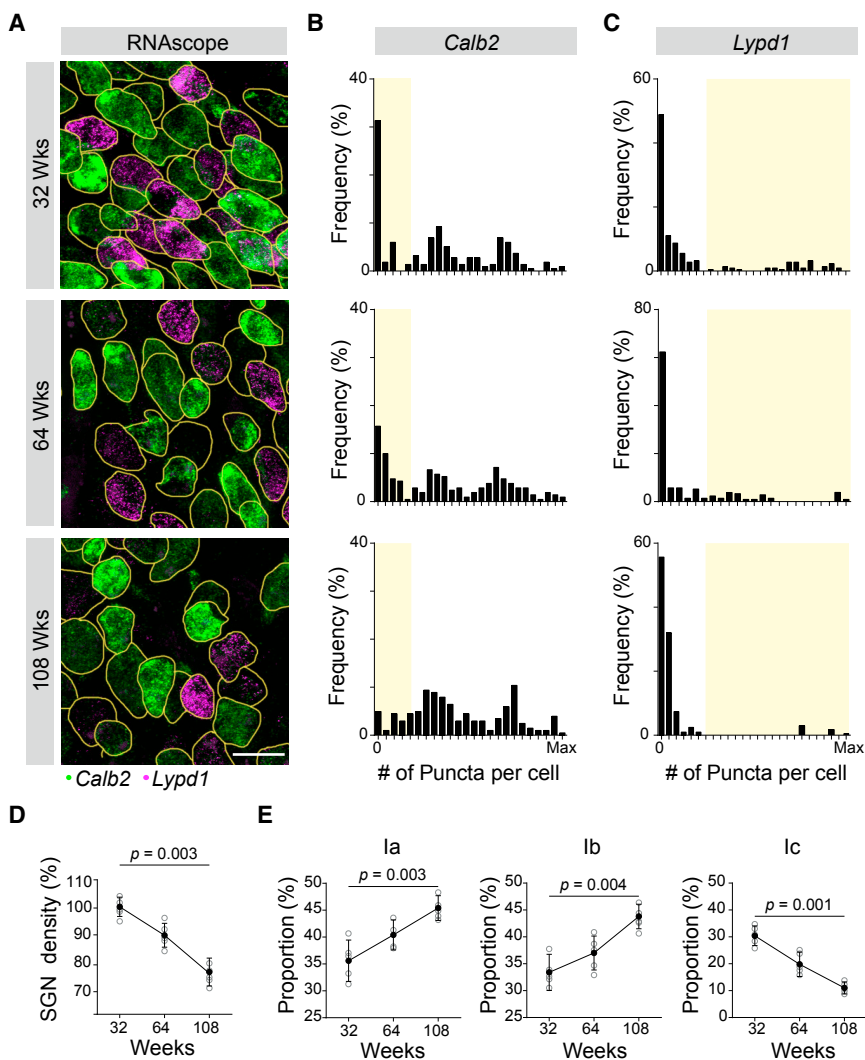


**Figure 5. Type I SGN Subtypes Show Differential Vulnerability to Age-Related Loss**

(A) SGN subtype identity was assessed using RNAcope to quantify levels of *Calb2* and *Lypd1* transcripts at 32, 64, and 108 weeks, shown in representative tissue sections.

(B and C) Histograms show the frequency distribution of *Calb2* (B) and *Lypd1* (C) mRNA levels for all analyzed SGNs at each age ( $n = 212$  cells, 5 animals at 32 weeks [top]; 175 cells, 5 animals at 64 weeks [middle]; 155 cells, 5 animals at 108 weeks [bottom]). The type Ic population, defined by low levels of *Calb2* and high levels of *Lypd1*, is shaded in yellow.

(D and E) SGN density (% relative to the 32-week time point) decreases over time (D), and this loss is matched with a decrease in the proportion of Ic SGNs (E). Types Ia and Ib SGNs increase in proportion over the same time frame, indicating that loss of Ic SGNs likely accounts for the overall decrease in density. Filled dots and error bars represent mean and SD, respectively.  $p$  values indicate results of Dunn's test following one-way ANOVA.

Scale bar, 10  $\mu$ m (A).

See also Figure S6 and Table S2.

(Figure 4J). Processes from neurons with medium CALB2 levels (Ib subtype) were flanked by high and low CALB2 processes (Ia and Ic subtypes, respectively) along the modiolar-pillar axis and were apposed to medium-sized synaptic ribbons. Overall, there was a strong positive correlation between CALB2 fiber intensity and synapse position ( $\rho = 0.72$ ) (Figure 4I) and a strong negative correlation ( $\rho = -0.70$ ) between CALB2 fiber intensity and the size of the associated ribbon (Figure 4J). Thus, Ia, Ib, and Ic fibers are topographically organized in the OSL and this order is preserved along the modiolar-pillar axis of the IHC, accompanied by a gradient of presynaptic ribbon size in IHCs (Figure 4K). Overall, based on fiber position, synapse location, and synapse morphology, the Ia, Ib, and Ic subtypes match the features of high-, medium- and low-SR subgroups, respectively.

#### Type Ic SGNs Are Selectively Vulnerable to Age-Related Loss

In aging animals, SGNs are progressively lost, and low-SR fibers are the most affected (Schmiedt et al., 1996; Sergeyenko et al., 2013). Thus, we assessed types Ia, Ib, and Ic SGNs in 32-, 64-,

and 108-week-old mice, as determined by expression of *Calb2* and *Lypd1* (Figures 5 and S6). SGN loss in aging animals was characterized by a gradual loss of cells expressing low levels of *Calb2* and high levels of *Lypd1* (Figure 5A), as evident in population histograms (Figures 5B and 5C) and scatterplots (Figure S6C). To assess the composition of SGNs at each stage, we defined *Calb2*<sup>hi</sup> *Lypd1*<sup>off</sup>, *Calb2*<sup>mid</sup> *Lypd1*<sup>off</sup>, and *Calb2*<sup>lo</sup> *Lypd1*<sup>hi</sup>

neurons as Ia, Ib, and Ic subtypes, respectively. As expected, overall SGN density declined with age (Figure 5D). Only type Ic SGNs showed a similar decrease, dropping from 30% at 32 weeks to 20% at 64 weeks and still further to 11% at 108 weeks (Figure 5E). The proportion of Ia and Ib SGNs increased. Thus, Ic SGNs are selectively vulnerable to age-related loss.

#### Signatures of SGN Subtypes Are Present at Birth and Refined over the First Postnatal Week

The discovery of molecularly distinct SGN subtypes raises the important question of how this heterogeneity is established in development. In many systems, identities are apparent as soon as neurons become post-mitotic, with additional activity-dependent modification as the neurons are integrated into functional circuits. In the mouse cochlea, type I and type II SGNs exhibit distinct anatomical features by E16.5 (Koundakjian et al., 2007). By contrast, variation among type I SGNs has not been detected until postnatal stages, after the peripheral processes have reached their IHC targets, and IHC-SGN synapse

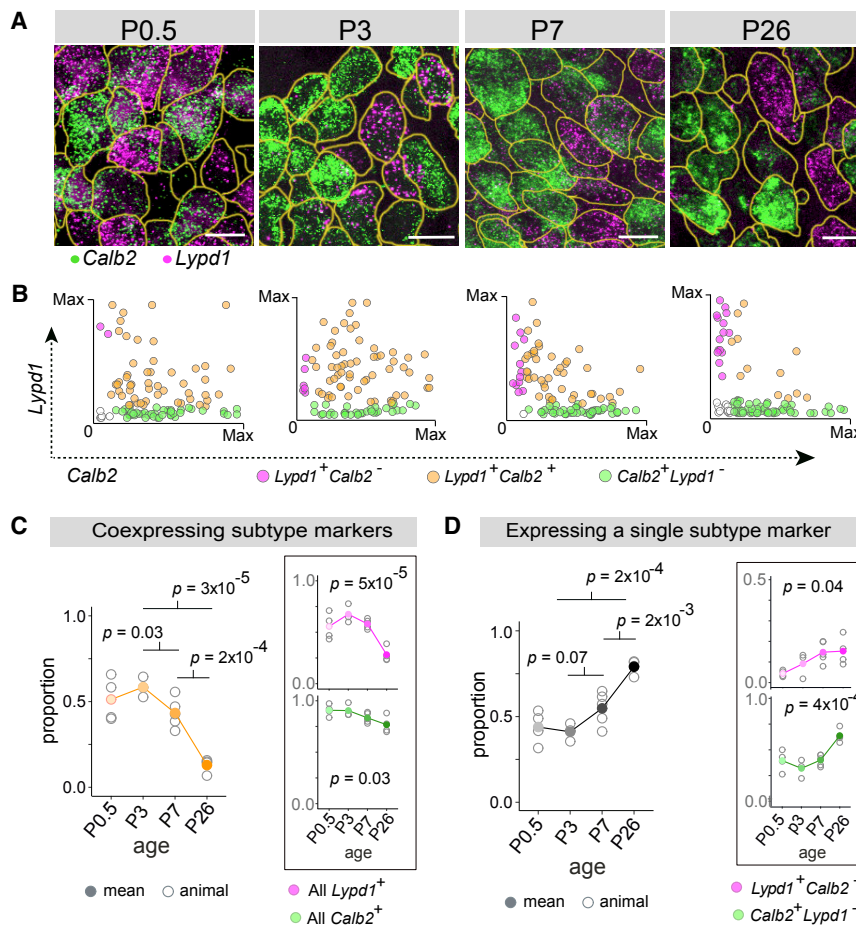


**Figure 6. Type I SGN Subtypes Gradually Emerge over the First Postnatal Week**

(A and B) Representative images of *Calb2* (green) and *Lypd1* (magenta) mRNA detected using RNAscope in tissue sections of cochlea at various developmental stages (A). Scatterplots (B) show expression levels of *Calb2* alone (green), *Lypd1* alone (magenta), or both markers (orange) in individual SGNs ( $n = 100$  randomly selected cells at each time point).

(C and D) Over time, the proportion of cells expressing both *Calb2* and *Lypd1* decreases (orange, B and C), shown also for expression of each gene individually (magenta and green, insets). In parallel, there is an increase in the proportion that express a single subtype marker (D), shown for the whole population (black), as well as separately for *Lypd1*<sup>+</sup> only SGNs (magenta, inset) and *Calb2*<sup>+</sup> only SGNs (green, inset). Means are shown in solid dots, with raw data from each individual animal in open circles.  $p$  values indicate results of Tukey's HSD test (left) and one-way ANOVA (right, inset). Scale bars, 10  $\mu$ m (A).

See also Figure S7 and Table S2.

morphology is not fully mature until the fourth postnatal week (Liberman and Liberman, 2016). Since the nature of the synapses linking IHCs to type I SGNs likely influences neuronal thresholds (Liberman et al., 2011), this relatively slow and late emergence of functional heterogeneity suggests that SGN subtype identity may not be fully established until the end of the first month of life. However, in the absence of a molecular toolkit, analysis of SGN development has been limited to young adult and adult stages, obscuring early developmental events that shape SGN identities.

Using subtype-specific markers, we found that SGNs begin to diversify perinatally, followed by a period of refinement over the first postnatal week (Figure 6). The Ia marker *Calb2* and Ic marker *Lypd1* are already expressed in SGNs by late embryonic stages (E18.5) and at P0.5, but sharply differ in breadth of expression: whereas *Calb2* is expressed in almost all neurons (>90%), *Lypd1* expression is more restricted (60%–70%) at both time points (Figures 6A and S7A–S7C). *Calb2* levels are relatively uniform at these early stages, unlike the strong variability observed in the mature cochlea (Figure 2J). Given the extensive co-expression and lack of a strong *Calb2* gradient, SGN identities cannot be assigned confidently. By P3, *Calb2* levels are more heterogeneous, and a small fraction of cells begin to show mutually exclusive expression of *Calb2* and *Lypd1*, with significantly more *Lypd1*<sup>+</sup>*Calb2*<sup>-</sup> neurons compared to P0.5 (Figure 6B,

magenta dots). The gradient of *Calb2* expression is even sharper at P7, and more low-*Calb2* or *Calb2*<sup>-</sup> neurons express high levels of *Lypd1*. At P26, *Calb2* and *Lypd1* show mutually exclusive expression in ~90% of SGNs (Figure 6D). These observations suggest that identities take shape through the gradual downregulation of *Calb2*, followed by maintenance of *Lypd1* in select SGNs.

Consistently, most SGNs initially express *Calb2*, but this proportion drops significantly after P3 ( $p = 0.03$ ) (Figure 6C, inset, green line). Expression of *Lypd1*, in comparison, first ramps up, possibly reflecting a slight delay in the onset of *Lypd1* relative to *Calb2*, and then decreases over time ( $p = 5 \times 10^{-5}$ ) (Figure 6C, inset, magenta line). These trends coincide with a sharp decline in the proportion of cells co-expressing subtype-specific markers both within the first postnatal week (P3 to P7:  $p = 0.03$ ) and over the first 3 weeks of postnatal development (P3 to P26,  $p = 3 \times 10^{-5}$ ) (Figure 6C, yellow line). At the same time, the proportion of cells expressing only one of the two markers increases (P3 to P26:  $p = 2 \times 10^{-4}$ ; P3 to P7:  $p = 0.07$ ) (Figure 6D). Thus, SGN molecular identities begin to take shape around birth, with broad and overlapping expression of markers that becomes progressively restricted and signs of adult-like mutually exclusive expression appearing by the end of the first postnatal week.

#### Synaptic Transmission from IHCs Is Necessary for SGN Diversification

Mice begin to respond to airborne sound around P12 and cochlear function continues to mature into the third postnatal week (Shnerson and Pujol, 1981). However, our data indicate that molecularly distinct SGNs emerge just after peripheral

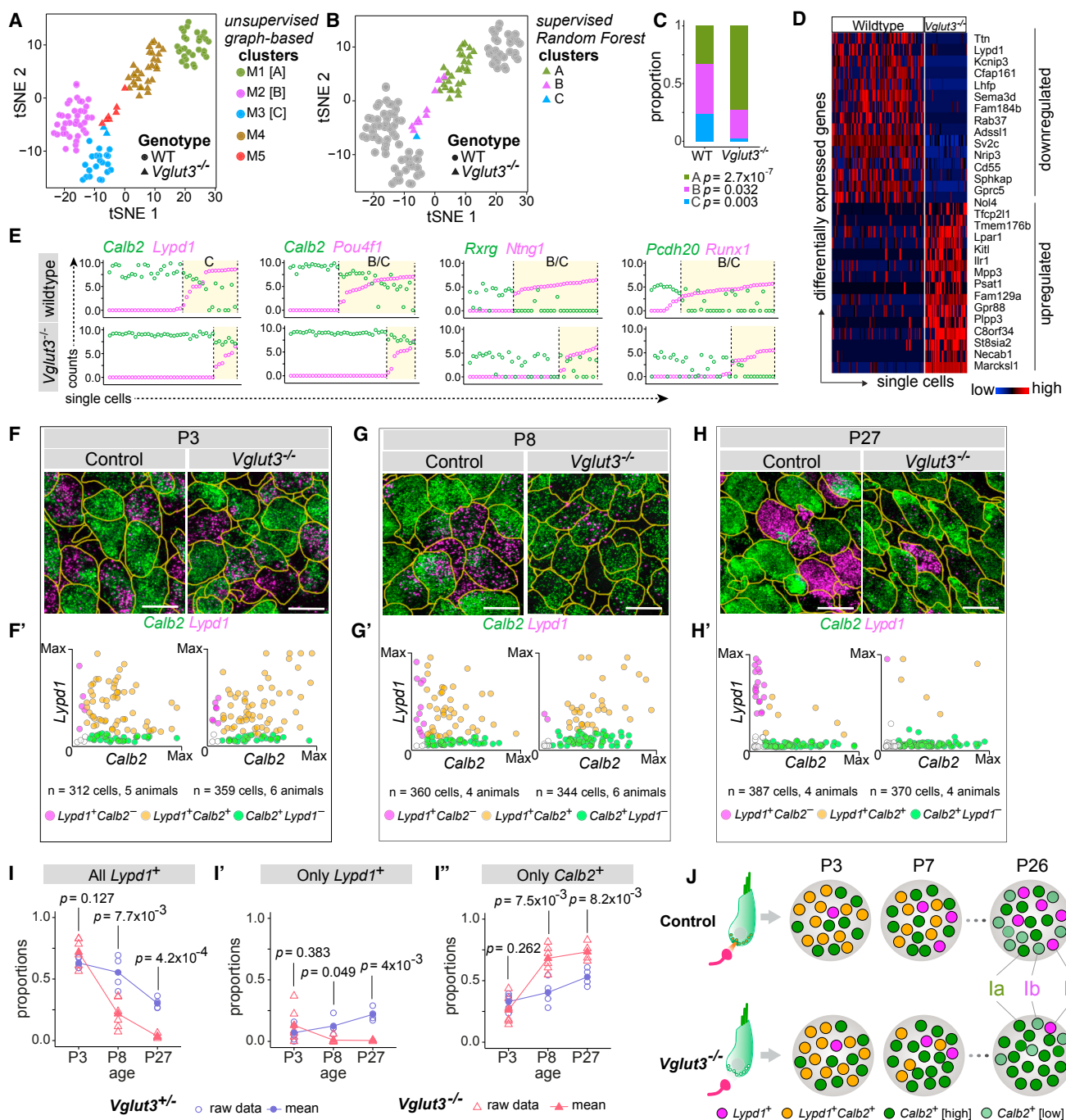


**Figure 7. SGN Heterogeneity Is Altered in a Mouse Model of Congenital Deafness**

(A) t-SNE embedding of single cell transcriptomic profiles from wild-type (WT, circles) and *Vglut3*<sup>-/-</sup> (triangles) animals, with five distinct clusters (M1–M5) predicted by graph-based unsupervised clustering indicated by color. M1, M2 and M3 correspond to WT Ia, Ib, and Ic SGNs, whereas M4 and M5 consist of SGNs from *Vglut3*<sup>-/-</sup> animals.

(B) Subtype identities of neurons from *Vglut3*<sup>-/-</sup> animals were assigned using supervised clustering by the Random Forest method. WT cells are shown in gray, and cells from *Vglut3*<sup>-/-</sup> animals are shown in colors corresponding to their predicted subtype identities. Cluster M4 (brown, A) consists of type Ia-like SGNs (green, B), whereas the remaining neurons in cluster M5 (red, A) are either more like type Ib (purple, B) or more like type Ic (blue, C) SGNs.

(C) Subtype proportions are significantly altered in *Vglut3*<sup>-/-</sup> animals compared to WT, with a dramatic loss of Ic SGNs. p values indicate results of test of equal proportions between Ia, Ib, and Ic subtypes in the two genetic backgrounds.

(legend continued on next page)

synapses begin to form at birth. To investigate whether synaptic communication influences SGN diversification, we performed scRNA-seq in P25-P27 *Vglut3*<sup>-/-</sup> mice, in which glutamatergic transmission from IHCs to SGNs is abolished. Transcriptional profiles of 40 SGNs from *Vglut3*<sup>-/-</sup> animals and 88 origin-matched wild-type SGNs were analyzed as described above. In a t-SNE plot, wild-type (WT) middle-turn SGNs again segregated into three distinct groups (Figure 7A). SGNs from *Vglut3*<sup>-/-</sup> animals, on the other hand, split into only two highly asymmetric groups. Unsupervised graph-based clustering sorted WT SGNs into three clusters (M1, M2, and M3), containing 33%, 43% and 24% of the cells, respectively. In contrast, 80% of *Vglut3*<sup>-/-</sup> SGNs formed a single cluster (M4), with the remaining 20% mostly in a small fifth cluster (M5). Based on expression of subtype-specific markers, WT cells in the M1, M2, and M3 clusters were identified as Ia, Ib, and Ic SGNs, respectively. The mutant cells in cluster M4 expressed Ia markers (such as *Calb2*) (Figure S7D), while those in M5 expressed mostly Ib markers (*Ntng1*, *Pou4f1*) and very low or zero levels of Ic markers (*Lypd1*, *Grm8*) (Figure S7D). Thus, the vast majority of SGNs (80%) from *Vglut3*<sup>-/-</sup> animals are Ia-like and the rest are Ib/Ic-like (20%).

To corroborate these results, we utilized Random Forest, an ensemble machine-learning approach, for supervised classification of *Vglut3*<sup>-/-</sup> cells based on subtype definitions derived from WT cells (Figure 7B). Importantly, this approach is independent of sample size. After verifying that the classifier performed robustly (Figures S7E–S7G; see the STAR Methods), predictions for SGNs from *Vglut3*<sup>-/-</sup> animals were generated (colored triangles in Figure 7B). We found that 73% of the mutant cells were transcriptionally similar to Ia SGNs, 25% were Ib-like, and 3% were Ic-like (Figure 7C). Consistent with the results of unsupervised classification, this indicated an overabundance of Ia-like neurons at the expense of Ib and Ic subtypes. Indeed, pooled comparison of scRNA-seq profiles of mutant and WT SGNs revealed a broad transcriptional shift toward the Ia phenotype, with downregulation of multiple Ib and Ic markers, such as *Ttn* and *Lypd1*, respectively (Figure 7D).

Variability in *Calb2* expression further supported this interpretation: *Calb2* levels ranged from moderate to high (standard deviation = 0.07) across all *Vglut3*<sup>-/-</sup> cells, as expected for a population comprised mostly of Ia SGNs. This contrasts with the steep gradient from zero to high expression observed among WT cells (standard deviation = 0.78) (Figure 7E). In addition,

*Lypd1* expression was limited to ~18% of cells, all of which lie near the WT Ib/Ic clusters in the t-SNE plot (Figure S7D). Changes in proportions of neurons expressing other Ib/Ic-specific or Ia-enriched transcription factors and axon guidance molecules (Figure 7E) are consistent with the interpretation that SGN subtypes are significantly altered in *Vglut3*<sup>-/-</sup> animals.

### Defective Consolidation of Ic Identity in *Vglut3*<sup>-/-</sup> Animals

Depolarization of IHCs triggers action potentials in SGNs, both in pre-hearing animals (<P12), when waves of spontaneous activity propagate from IHCs to SGNs and up the auditory axis, and in post-hearing animals, when IHC-SGN transmission is essential for mEPSCs and sound-evoked action potentials. The change in SGN proportions seen in *Vglut3*<sup>-/-</sup> animals could arise from disruption of activity at either stage. To determine when SGN diversification goes awry, we examined expression of subtype-specific markers at earlier developmental stages. At P3, both *Calb2* and *Lypd1* are expressed in the expected proportion of SGNs in *Vglut3*<sup>-/-</sup> animals compared to WT (all *Lypd1*<sup>+</sup> SGNs: 0.63 and 0.72, p = 0.13; only *Lypd1*<sup>+</sup> SGNs: 0.07 and 0.13, p = 0.38; only *Calb2*<sup>+</sup> SGNs: 0.33 and 0.26, p = 0.26 in control and *Vglut3*<sup>-/-</sup>, respectively) (Figures 7F, 7F', and 7I–I"). Thus, the onset of subtype specification does not require IHC-driven activity. However, by P8, the proportion of cells expressing the Ic marker *Lypd1* is decreased significantly in *Vglut3*<sup>-/-</sup> animals (All *Lypd1*<sup>+</sup> SGNs: 0.55 and 0.22, p = 7.7 × 10<sup>-3</sup>; only *Lypd1*<sup>+</sup> SGNs: 0.13 and 0.01, p = 0.049 in control and *Vglut3*<sup>-/-</sup>, respectively) (Figure 7G, 7G', 7I, and 7I'). This is accompanied by an increased proportion of *Calb2*<sup>+</sup> SGNs (only *Calb2*<sup>+</sup> SGNs: 0.40 and 0.68, p = 7.5 × 10<sup>-3</sup> in control and *Vglut3*<sup>-/-</sup>, respectively) (Figure 7I"). These changes persist into the fourth postnatal week (Figures 7H and 7H'), with significantly lower *Lypd1*<sup>+</sup> SGN proportion at P27 in *Vglut3*<sup>-/-</sup> animals (All *Lypd1*<sup>+</sup> SGNs: 0.30 and 0.03, p = 4.2 × 10<sup>-4</sup>; only *Lypd1*<sup>+</sup> SGNs: 0.22 and 0.007, p = 4 × 10<sup>-3</sup> in control and *Vglut3*<sup>-/-</sup>, respectively) (Figure 7I and 7I'), consistent with scRNA-seq results (Figures 7A–7E).

Comparison of marker expression over time suggests that *Vglut3*<sup>-/-</sup> animals fail to produce Ib/c subtypes from among a pool of SGNs with mixed identity, which instead assume Ia identities. In control animals, the proportion of *Lypd1*<sup>+</sup> SGNs decreases modestly (~13%) between P3 and P8 (Figure 7I, blue line), consistent with the expected gradual refinement of SGN

(D and E) SGNs from WT and *Vglut3*<sup>-/-</sup> animals show broad differences in gene expression reflective of a shift from Ic to Ia identity, shown both in a heatmap (D) and in scatterplots (E) of the level of expression of Ia (*Calb2*, *Rxrg*, *Pcdh20*) and Ib/Ic (*Lypd1*, *Pou4f1*, *Ntng1*, *Runx1*) subtype markers (WT, top; *Vglut3*<sup>-/-</sup>, bottom). Yellow shading represents cells belonging to B/C or C clusters.

(F–H) RNAscope of tissue sections from P3 (F), P8 (G), and P27 (H) WT (left) and *Vglut3*<sup>-/-</sup> (right) animals shows that expression of *Calb2* (green) and *Lypd1* (magenta) initiates normally at P3, quantified in (F'). However, the proportion of *Lypd1*<sup>+</sup> SGNs is lower in *Vglut3*<sup>-/-</sup> animals at P8 (G'), and almost no *Lypd1*<sup>+</sup> SGNs remain at P27 (H'). Scatterplots (F'–H') show individual cells expressing *Calb2* alone (green), *Lypd1* alone (magenta), or co-expressing both markers (orange). In each plot, 100 randomly selected cells are shown for clarity.

(I–I") Proportions of SGNs in control (blue circles) and *Vglut3*<sup>-/-</sup> (red triangles) animals that express any *Lypd1* (I), that express only *Lypd1* (I'), or that express only *Calb2* (I"). Means are shown in solid symbols, with raw data from individual animals in open symbols. p values refer to results of independent samples t test between the two genetic backgrounds at each time point.

(J) Schematic showing developmental emergence of mutually exclusive expression between *Calb2* and *Lypd1*. In *Vglut3*<sup>-/-</sup> animals, in which glutamate release from IHCs is abolished, *Lypd1*<sup>+</sup> SGNs are severely underrepresented compared to control animals, beginning after P3, resulting in overabundance of Ia SGNs by the fourth postnatal week.

Scale bars, 10 μm (F–H).

See also Figure S7 and Table S2.

identities (Figure 6). However, in *Vglut3*<sup>-/-</sup> animals, the proportion of *Lypd1*<sup>+</sup> SGNs drops drastically (~70%) (Figure 7I, red line). This is unlikely to reflect accelerated maturation because the proportions continue to decrease to near-absence of *Lypd1*<sup>+</sup> SGNs by P27 (~96% versus P3, in contrast to ~52% in control). At the same time, the proportion of SGNs that express only *Lypd1*<sup>+</sup> (and not *Calb2*) does not increase over time, in contrast to controls (Figure 7I'). Instead, the proportion of *Calb2*<sup>+</sup>-only SGNs increases between P3 and P8 to a much greater extent in *Vglut3*<sup>-/-</sup> animals (+161%) than in controls (+21%) (Figure 7I"). Thus, in *Vglut3*<sup>-/-</sup> animals, the *Calb2* gradient does not sharpen and there is a dramatic loss in *Lypd1* expression, as if most remaining SGNs retained a la identity rather than taking on a lb/c identity in the first postnatal week and beyond (Figure 7J).

Thus, our data indicate that IHC-driven activity is required for the developmental refinement of SGN identities from an early phase of broad and overlapping marker expression to subtype-restricted expression, with impairment of this process causing a drastic shift in SGN subtype proportions within the first postnatal week, which persists in the mature cochlea (Figure 7J).

## DISCUSSION

SGNs enable the wide dynamic range needed to sense sounds from the rustle of a leaf to the roar of a jet engine. Although SGNs show well-characterized differences in morphological and functional properties that subserve dynamic range expansion (Kawase and Liberman, 1992; Liberman, 1982, 1991; Liberman et al., 2011; Taberner and Liberman, 2005), the molecular correlates of such heterogeneity have been a mystery. Using single-cell transcriptomics in mice, we define three subtypes of type I SGNs that match the anatomical features of those originally defined by physiology, including the subtype preferentially affected by age-related loss. These SGN subtypes express distinct cohorts of ion channels, receptors, synaptic proteins, and adhesion molecules that vary both locally and along the tonotopic axis, indicating that a complex reservoir of SGNs is available for coding auditory information. Unexpectedly, SGNs with distinct identities emerge during the first postnatal week in an activity-dependent manner. Together, these results establish a new molecular logic for cochlear circuitry, reveal the potential for many endogenous differences among SGNs, and suggest a new model for when and how SGN diversification is achieved, with important implications for the treatment of congenital deafness.

It was not a given that SGNs could be parsed molecularly, since the response properties that differentiate them could be entirely imposed by other cells in the circuit, e.g., functional presynaptic differences within IHCs (Wichmann and Moser, 2015) or differential innervation by olivocochlear efferents (Yin et al., 2014). To the contrary, we find that individual SGNs are intrinsically different in ways that could fundamentally alter their input and output properties. For instance, each subtype expresses unique cohorts of K<sup>+</sup> channel subunits, Na<sup>+</sup> channel subunits, and Ca<sup>2+</sup>-binding proteins that could yield distinct responses to input from IHCs and efferent neurons, such that both endogenous and circuit-level differences underlie SR-group heterogeneity.

Notably, one of the most robust markers for Ic SGNs is *Lypd1*, which encodes a transmembrane receptor implicated in cholinergic signaling (Tekinay et al., 2009). Thus, type Ic SGNs may exhibit unique responses to acetylcholine released by olivocochlear efferents. However, *Lypd1* is only one of many class-specific genes that could create other, as yet uncharacterized, diversity in SGN electrical properties beyond SR and threshold. For instance, types Ib and Ic SGNs are similar at the molecular level, suggesting they might be difficult to distinguish physiologically and highlighting the need for other means of classification. Similarly, whole-cell recordings from immature type I somata reveal a range of electrical properties (Crozier and Davis, 2014; Liu et al., 2014), some of which depend on voltage-gated K<sup>+</sup> channels (Liu et al., 2014) or correlate with levels of Ca<sup>2+</sup>-binding proteins (Liu and Davis, 2014). Given this broad range of possible physiological differences, SR differences are unlikely to be explained by single genes, and other variable features may also contribute to auditory coding in ways we do not yet understand.

SGNs may also differ in how they transmit signals to their brainstem targets in the cochlear nucleus complex (CNC). Types Ia, Ib, and Ic SGNs express distinct complements of axonal molecules, including proteins associated with presynaptic terminals such as the metabotropic glutamate receptor *Grm8* and the exocytosis regulator *Cpx2*. Such molecular differences could generate distinct modes of plasticity and presynaptic release centrally, consistent with suggestions that presynaptic release is not uniform in the CNC (Cao and Oertel, 2010). Given the differences in expression of presynaptic molecules, as well as cell-adhesion molecules, such as the Netrin family gene *Ntng1*, SGN subtypes may stimulate separate networks of CNC targets by virtue of their unique synaptic properties and connectivity. Indeed, previous studies have revealed both mixed and selective innervation of central targets by different SR groups. Multipolar cells in one part of the anteroventral cochlear nucleus (AVCN) receive inputs from all SR groups, whereas multipolar cells in another part of the AVCN, and in the small-cell cap region, are almost exclusively innervated by low- and medium-SR fibers (Liberman, 1991; Ryugo, 2008).

With the discovery of molecular differences among type I SGNs comes the opportunity to not only test long-standing hypotheses but also pursue fresh questions regarding their functional properties and significance. Much has been learned about the physiology of type I SGNs in adult ears via single-fiber recordings from the VIII<sup>th</sup> nerve, work that showed correlations between SR and numerous other physiological features, as well as vulnerability to aging and noise damage. Our results make it possible to further elucidate the features and functions of individual subtypes, for instance by assessing the circuit-level contributions of each subtype to auditory behavior by using genetic approaches to perform targeted ablations. Some caution is warranted before embarking on such studies, however, due to the broad distribution of subtype-specific markers early in development. Careful consideration of expression dynamics will be critical for obtaining interpretable results. In this regard, combining subtype-specific markers with approaches that permit precise spatiotemporal control of gene expression, for instance via intersectional targeting strategies, may prove useful. Our data also

stimulate new hypotheses regarding the mechanistic basis of SGN physiology, including, but not limited to, SR. Because of the technical difficulties of recording from individual adult SGNs both *in vivo* and *in vitro*, it will take time to work out how individual molecules contribute to SGN subtype function and ultimately hearing. Indeed, the breadth of molecular differences uncovered here identifies new questions beyond the origins of SR heterogeneity and opens many doors that could fuel the field for years to come.

### Multiple Layers of Tonotopic Variation among Type I SGNs

Tonotopy is a fundamental organizing principle in the auditory system that originates with the orderly gradient of frequency tuning along the cochlear spiral. Although emphasis is placed on this frequency axis and the gradient in hair cell mechanics that underlies it, tonotopic differences in SGN physiology have also been described, such as differences in action potential kinetics at neonatal stages (Adamson et al., 2002). However, with only a few genes identified (Adamson et al., 2002; Flores-Otero and Davis, 2011), neither the origin nor the extent of such variation is clear. Our results reveal differences in molecules spanning diverse gene families across the tonotopic axis. Many are involved in neuronal connectivity, such as the Ephrin gene *Efna1*, and might therefore help maintain topographic organization within the VIII<sup>th</sup> nerve and in the CNC. Others could influence SGN physiology, such as the K<sup>+</sup> channel subunit *Kcns3*, as well as *Cacng5*, *Cpne6*, and *Vamp2*. Thus, rather than serving as identical conduits within a topographically ordered circuit, SGNs may exhibit endogenous differences in their response properties that affect encoding of low versus high sound frequencies. Intriguingly, some tonotopic variation was limited to individual SGN subtypes, such that there could be three overlapping maps along the cochlear spiral. Nonetheless, the difference across subtypes, rather than tonotopic variation, was the dominant form of molecular heterogeneity in the adult cochlea. This suggests that the ear's dynamic range is extended by the development of molecularly distinct cohorts of SGNs that are further specialized based on their tonotopic position.

Detection of complex sounds can depend not only on the properties and connectivity of SGN subtypes but also on the proportions of these subtypes along the tonotopic axis. Interestingly, the distribution of SR rates is uniform in some species (Liberman, 1978; Tsuji and Liberman, 1997), whereas others show striking differences across the tonotopic axis (Schmid, 1989). The situation in mice is ambiguous, since it is more difficult to record from large populations of SGNs in such small animals (Taberner and Liberman, 2005). Here, we find a larger proportion of Ia neurons and smaller proportion of Ib neurons in the base compared to the rest of the cochlea. Such regional variation could enable heightened responses to certain, ethologically relevant sound frequencies, much as the presence of a high cone:rod photoreceptor ratio in the fovea of the retina enables strong color perception (Curcio and Hendrickson, 1991). Thus, SGNs could contribute to stimulus coding at multiple levels, from cell-based differences within and across SGN classes to tissue-level differences in their pattern of distribution along the cochlear spiral.

### SGN Subtypes Emerge Early via an Activity-Dependent Process

The presence of molecular SGN subtypes presents a challenge for wiring the developing cochlea, where one IHC connects to 10–30 SGNs that share the same basic patterns of connectivity and also exhibit diverse anatomical and functional phenotypes (Liberman, 1982; Liberman et al., 2011). Heterogeneity in the size of postsynaptic glutamate receptor patches is detectable by P14 in mice, but other features, such as synapse number, efferent innervation density, ribbon size gradient, and ion channel localization, reach maturity only between the third and fourth postnatal weeks (Kim and Rutherford, 2016; Liberman and Liberman, 2016). Therefore, it was surprising that Ib/Ic markers appear in subsets of SGNs shortly after their processes reach hair cells around E15.5 (Koundakjian et al., 2007), and that well-defined subtypes emerge coincident with a period of synaptogenesis and pruning during the first postnatal week (Huang et al., 2012; Meyer et al., 2009). Thus, SGN diversity is seeded soon after they form connections, pointing to a major role for signaling between IHCs and SGNs in the acquisition of mature identities.

Although mature type I SGNs express class-specific genes, these differences emerge after several days of co-expression (Figure 6). Transition from such a mixed state is defined by a singular rule: those that maintain Ib/Ic-specific genes lose Ia identity and those that do not continue as Ia neurons. Although transient periods of co-expression are a recurrent theme in the developing nervous system, conflicting identities are typically resolved intrinsically, for instance, by mutual repression of class-specific transcription factors within individual progenitors (Jukam and Desplan, 2010). SGN identity, on the other hand, appears to be shaped by neuronal activity. When IHCs can no longer release glutamate to activate SGNs, as occurs in *Vglut3*<sup>-/-</sup> animals (Seal et al., 2008), the proportion of Ib/Ic SGNs is drastically decreased. Since markers for Ib/Ic SGNs appear normally at P3 in these animals, activity seems to bias how the mixed state is ultimately resolved, rather than directly specifying Ib/Ic identity. Furthermore, additional unbiased transcriptional profiling in *Vglut3*<sup>-/-</sup> animals confirmed that most SGNs assume a nearly normal Ia identity. Thus, IHC-driven activity appears to select a subset of SGNs to take on Ib and Ic fates from a pool of SGNs that would otherwise become Ia.

Although we have focused on IHC-driven events, any change in cochlear activity may also contribute to the final mix of SGNs. Indeed, SGN activity in the neonatal cochlea depends not only on IHCs but also on input from the olivocochlear efferent system. For example, medial efferents form transient cholinergic synapses with IHCs during the first postnatal week (Glowatzki and Fuchs, 2000) and are thus poised to influence IHC-evoked SGN activity during this period of SGN diversification. Lateral efferents could also influence SGN identity, perhaps in a maintenance role as suggested previously (Yin et al., 2014). In this issue of *Cell*, Sun et al. (2018) also report that type I SGNs can be classified into three broad molecular subtypes that match those we describe here. Consistent with our findings, they demonstrate that subtype-specific marker expression changes upon disruption of mechanotransduction (*TmIE*<sup>-/-</sup>) or glutamate release from IHCs (*Vglut3*<sup>-/-</sup>), both of which significantly alter SGN

spontaneous activity patterns. Regardless of which factors pattern SGN activity during this critical developmental window, their effects may materialize as changes in expression or function of subtype-specific transcription factors, such as *Pou4f1* and *Runx1*. In fact, both *Pou4f1* and *Runx1* contribute to diversification of dorsal root ganglion neurons (Chen et al., 2006; Qi et al., 2017; Yoshikawa et al., 2007; Zou et al., 2012) and could play similar roles in SGNs, acting downstream of a generic differentiation program headed by the master regulator *Gata3* (Appler et al., 2013; Yu et al., 2013). Interestingly, a similar activity-dependent mechanism diversifies cortical interneurons with distinct firing properties, in this case via the transcription factor *Er81* (Dehorter et al., 2015). Such a mechanism of neuronal diversification may be particularly effective in the cochlea, where patterns of IHC-driven activity during an early plastic phase, achieved for instance via efferent modulation, could yield mature subtype proportions across the cochlea from a finite pool of generic postmitotic neurons. Under this model, SGN heterogeneity is established by both intrinsic and extrinsic mechanisms: presynaptically patterned activity informs identity during development, yet the SGNs also express transcription factors that induce and maintain subtype-specific cohorts of genes to further shape each neuron's mature functional properties. An important question for the future is whether SGN identities remain sensitive to activity into adulthood or whether these early developmental events lock them in place.

### Implication for Disease and Therapy

Loss of *Vglut3* causes total deafness in mice (Seal et al., 2008), while mutation in *Vglut3* underlies the deafness DFNA25 in humans (Ruel et al., 2008). Therefore, a major implication of the influence of IHC-driven activity on SGN identity is that some forms of congenital deafness—specifically those that disrupt SGN activity before the onset of hearing—may have an associated SGN pathology. This underscores the need to look beyond the primary molecular lesion in assessments of cellular phenotypes associated with deafness-causing mutations. An outstanding question is whether restoring expression of a defective gene in IHCs is sufficient to correct the sequelae of SGN phenotypes associated with a congenital lesion. The answer lies in part in whether plasticity of SGN identity, particularly its susceptibility to extrinsic influence, persists into adulthood. Should it be necessary to directly target SGNs to re-establish correct proportions, valuable insights may be gained from studies focusing on molecular genetic regulation of SGN subtype identity during development and beyond.

### STAR★METHODS

Detailed methods are provided in the online version of this paper and include the following:

- KEY RESOURCES TABLE
- CONTACT FOR REAGENT AND RESOURCE SHARING
- EXPERIMENTAL MODEL AND SUBJECT DETAILS
  - Mice
- METHOD DETAILS
  - Single cell RNA-sequencing

- Tissue processing for mRNA/protein detection
- QUANTIFICATION AND STATISTICAL ANALYSIS
  - Sequencing and bioinformatic analysis
  - Image acquisition and analysis
- DATA AND SOFTWARE AVAILABILITY

### SUPPLEMENTAL INFORMATION

Supplemental Information includes seven figures and two tables and can be found with this article online at <https://doi.org/10.1016/j.cell.2018.07.007>.

### ACKNOWLEDGMENTS

We thank Dr. Sinisa Hrvatin (Harvard) for help with sequencing and helpful discussions; Dr. Aravind Parthasarathy and Karina Gaft (MEEI) for help with processing the aged cochleas; Jocelyn Curran and Laura Schell (Harvard) for technical help; Rory Kirchner (Harvard) for input on bioinformatics; the Image and Data Analysis Core (IDAC, Harvard) for guidance on image analysis; Dr. Filippo Rijli (FMI, Switzerland) for sharing *Mafb*<sup>CreERT2</sup>;Ai9 mice; and Drs. David Corey and Michael Greenberg (Harvard) for sharing equipment. We also thank Drs. Matthew Kelley (NIDCD) and Ulrich Mueller (Johns Hopkins) for communicating their preliminary results and Drs. Matthew Kelley, David Ginty, and Gord Fishell and lab members (Harvard) for their critical reading of the manuscript. Bioinformatic analysis was partly conducted on the Orchestra High Performance Computing Cluster (Harvard), a resource partially supported through a grant from the NCRR (1S10RR028832-01). This work was supported by a Edward R. and Anne G. Lefler Research Grant (to L.V.G.), a Harvard Brain Science Initiative Collaborative Seed Grant (to L.V.G.), a Leonard and Isabelle Goldenson Postdoctoral Fellowship (to B.R.S.), and the NIH (T32 AG 222-24 to C.C., 5 T32 NS007484-14 and 5F32DC014371 to B.R.S., R01 DC000188 to M.C.L., and DC009223 to L.V.G.).

### AUTHOR CONTRIBUTIONS

B.R.S. and L.V.G. conceived of the study. B.R.S., C.C., and L.W. performed the experiments. B.R.S. and C.C. analyzed the data. S.G.K. provided animals. M.C.L. assisted with the design and interpretation of the experiments. B.R.S. and L.V.G. wrote the manuscript, with input from M.C.L.

### DECLARATION OF INTERESTS

The authors declare no competing interests.

Received: February 12, 2018

Revised: April 23, 2018

Accepted: July 2, 2018

Published: August 2, 2018

### REFERENCES

- Abraira, V.E., and Ginty, D.D. (2013). The sensory neurons of touch. *Neuron* 79, 618–639.
- Adamson, C.L., Reid, M.A., Mo, Z.L., Bowne-English, J., and Davis, R.L. (2002). Firing features and potassium channel content of murine spiral ganglion neurons vary with cochlear location. *J. Comp. Neurol.* 447, 331–350.
- Appler, J.M., Lu, C.C., Druckenbrod, N.R., Yu, W.-M., Koundakjian, E.J., and Goodrich, L.V. (2013). *Gata3* is a critical regulator of cochlear wiring. *J. Neurosci.* 33, 3679–3691.
- Berglund, A.M., and Ryugo, D.K. (1987). Hair cell innervation by spiral ganglion neurons in the mouse. *J. Comp. Neurol.* 255, 560–570.
- Borg, E., Engström, B., Linde, G., and Marklund, K. (1988). Eighth nerve fiber firing features in normal-hearing rabbits. *Hear. Res.* 36, 191–201.
- Brown, M.C. (1987). Morphology of labeled afferent fibers in the guinea pig cochlea. *J. Comp. Neurol.* 260, 591–604.

- Butler, A., Hoffman, P., Smibert, P., Papalex, E., and Satija, R. (2018). Integrating single-cell transcriptomic data across different conditions, technologies, and species. *Nat. Biotechnol.* 36, 411–420.
- Cao, X.-J., and Oertel, D. (2010). Auditory nerve fibers excite targets through synapses that vary in convergence, strength, and short-term plasticity. *J. Neurophysiol.* 104, 2308–2320.
- Chen, C.L., Broom, D.C., Liu, Y., de Nooij, J.C., Li, Z., Cen, C., Samad, O.A., Jessell, T.M., Woolf, C.J., and Ma, Q. (2006). Runx1 determines nociceptive sensory neuron phenotype and is required for thermal and neuropathic pain. *Neuron* 49, 365–377.
- Chen, W.C., Xue, H.Z., Hsu, Y.L., Liu, Q., Patel, S., and Davis, R.L. (2011). Complex distribution patterns of voltage-gated calcium channel  $\alpha$ -subunits in the spiral ganglion. *Hear. Res.* 278, 52–68.
- Costalupes, J.A., Young, E.D., and Gibson, D.J. (1984). Effects of continuous noise backgrounds on rate response of auditory nerve fibers in cat. *J. Neurophysiol.* 51, 1326–1344.
- Crozier, R.A., and Davis, R.L. (2014). Unmasking of spiral ganglion neuron firing dynamics by membrane potential and neurotrophin-3. *J. Neurosci.* 34, 9688–9702.
- Curcio, C.A., and Hendrickson, A.E. (1991). Organization and development of the primate photoreceptor mosaic. *Prog. Retinal Res.* 10, 89–120.
- Dehorter, N., Ciceri, G., Bartolini, G., Lim, L., Del Pino, I., and Marín, O. (2015). Tuning of fast-spiking interneuron properties by an activity-dependent transcriptional switch. *Science* 349, 1216–1220.
- Di Meglio, T., Kratochwil, C.F., Vilain, N., Loche, A., Vitobello, A., Yonehara, K., Hrycaj, S.M., Roska, B., Peters, A.H.F.M., Eichmann, A., et al. (2013). Ezh2 orchestrates topographic migration and connectivity of mouse precerebellar neurons. *Science* 339, 204–207.
- Echteler, S.M., and Nofsinger, Y.C. (2000). Development of ganglion cell topography in the postnatal cochlea. *J. Comp. Neurol.* 425, 436–446.
- Edgar, R., Domrachev, M., and Lash, A.E. (2002). Gene Expression Omnibus: NCBI gene expression and hybridization array data repository. *Nucleic Acids Res.* 30, 207–210.
- elBarbary, A. (1991). Auditory nerve of the normal and jaundiced rat. I. Spontaneous discharge rate and cochlear nerve histology. *Hear. Res.* 54, 75–90.
- Flores, E.N., Duggan, A., Madathany, T., Hogan, A.K., Márquez, F.G., Kumar, G., Seal, R.P., Edwards, R.H., Liberman, M.C., and García-Añoveros, J. (2015). A non-canonical pathway from cochlea to brain signals tissue-damaging noise. *Curr. Biol.* 25, 606–612.
- Flores-Otero, J., and Davis, R.L. (2011). Synaptic proteins are tonotopically graded in postnatal and adult type I and type II spiral ganglion neurons. *J. Comp. Neurol.* 519, 1455–1475.
- Frank, T., Khimich, D., Neef, A., and Moser, T. (2009). Mechanisms contributing to synaptic  $\text{Ca}^{2+}$  signals and their heterogeneity in hair cells. *Proc. Natl. Acad. Sci. USA* 106, 4483–4488.
- Furman, A.C., Kujawa, S.G., and Liberman, M.C. (2013). Noise-induced cochlear neuropathy is selective for fibers with low spontaneous rates. *J. Neurophysiol.* 110, 577–586.
- Glowatzki, E., and Fuchs, P.A. (2000). Cholinergic synaptic inhibition of inner hair cells in the neonatal mammalian cochlea. *Science* 288, 2366–2368.
- Glowatzki, E., and Fuchs, P.A. (2002). Transmitter release at the hair cell ribbon synapse. *Nat. Neurosci.* 5, 147–154.
- Guinan, J.J., Jr. (2018). Olivocochlear efferents: Their action, effects, measurement and uses, and the impact of the new conception of cochlear mechanical responses. *Hear. Res.* 362, 38–47.
- Huang, L.C., Barclay, M., Lee, K., Peter, S., Housley, G.D., Thorne, P.R., and Montgomery, J.M. (2012). Synaptic profiles during neurite extension, refinement and retraction in the developing cochlea. *Neural Dev.* 7, 38.
- Jukam, D., and Desplan, C. (2010). Binary fate decisions in differentiating neurons. *Curr. Opin. Neurobiol.* 20, 6–13.
- Kawase, T., and Liberman, M.C. (1992). Spatial organization of the auditory nerve according to spontaneous discharge rate. *J. Comp. Neurol.* 319, 312–318.
- Kiang, N.Y., Watanabe, T., Thomas, E.C., and Clark, L.F. (1965). Discharge Patterns of Single Fibers in the Cat's Auditory Nerve (MIT Press).
- Kiang, N.Y.S., Sachs, M.B., and Peake, W.T. (1967). Shapes of tuning curves for single auditory-nerve fibers. *J. Acoust. Soc. Am.* 42, 1341–1342.
- Kim, K.X., and Rutherford, M.A. (2016). Maturation of NaV and KV channel topographies in the auditory nerve spike initiator before and after developmental onset of hearing function. *J. Neurosci.* 36, 2111–2118.
- Koundakjian, E.J., Appler, J.L., and Goodrich, L.V. (2007). Auditory neurons make stereotyped wiring decisions before maturation of their targets. *J. Neurosci.* 27, 14078–14088.
- Liberman, M.C. (1978). Auditory-nerve response from cats raised in a low-noise chamber. *J. Acoust. Soc. Am.* 63, 442–455.
- Liberman, M.C. (1980). Efferent synapses in the inner hair cell area of the cat cochlea: an electron microscopic study of serial sections. *Hear. Res.* 3, 189–204.
- Liberman, M.C. (1982). Single-neuron labeling in the cat auditory nerve. *Science* 216, 1239–1241.
- Liberman, M.C. (1991). Central projections of auditory-nerve fibers of differing spontaneous rate. I. Anteroventral cochlear nucleus. *J. Comp. Neurol.* 313, 240–258.
- Liberman, M.C. (2017). Noise-induced and age-related hearing loss: new perspectives and potential therapies. *F1000Res.* 6, 927.
- Liberman, L.D., and Liberman, M.C. (2016). Postnatal maturation of auditory-nerve heterogeneity, as seen in spatial gradients of synapse morphology in the inner hair cell area. *Hear. Res.* 339, 12–22.
- Liberman, L.D., Wang, H., and Liberman, M.C. (2011). Opposing gradients of ribbon size and AMPA receptor expression underlie sensitivity differences among cochlear-nerve/hair-cell synapses. *J. Neurosci.* 31, 801–808.
- Liu, W., and Davis, R.L. (2014). Calretinin and calbindin distribution patterns specify subpopulations of type I and type II spiral ganglion neurons in postnatal murine cochlea. *J. Comp. Neurol.* 522, 2299–2318.
- Liu, Q., Lee, E., and Davis, R.L. (2014). Heterogeneous intrinsic excitability of murine spiral ganglion neurons is determined by Kv1 and HCN channels. *Neuroscience* 257, 96–110.
- Madisen, L., Zwingman, T.A., Sunkin, S.M., Oh, S.W., Zariwala, H.A., Gu, H., Ng, L.L., Palmiter, R.D., Hawrylycz, M.J., Jones, A.R., et al. (2010). A robust and high-throughput Cre reporting and characterization system for the whole mouse brain. *Nat. Neurosci.* 13, 133–140.
- Mann, Z.F., and Kelley, M.W. (2011). Development of tonotopy in the auditory periphery. *Hear. Res.* 276, 2–15.
- Meyer, A.C., Frank, T., Khimich, D., Hoch, G., Riedel, D., Chapochnikov, N.M., Yarin, Y.M., Harke, B., Hell, S.W., Egner, A., and Moser, T. (2009). Tuning of synapse number, structure and function in the cochlea. *Nat. Neurosci.* 12, 444–453.
- Nishimura, K., Noda, T., and Dabdoub, A. (2017). Dynamic expression of Sox2, Gata3, and Prox1 during primary auditory neuron development in the mammalian cochlea. *PLoS ONE* 12, e0170568.
- Picelli, S., Björklund, Å.K., Faridani, O.R., Sagasser, S., Winberg, G., and Sandberg, R. (2013). Smart-seq2 for sensitive full-length transcriptome profiling in single cells. *Nat. Methods* 10, 1096–1098.
- Qi, L., Huang, C., Wu, X., Tao, Y., Yan, J., Shi, T., Cao, C., Han, L., Qiu, M., Ma, Q., et al. (2017). Hierarchical specification of pruriceptors by Runt-domain transcription factor Runx1. *J. Neurosci.* 37, 5549–5561.
- Ross, S.E., Mardinly, A.R., McCord, A.E., Zurawski, J., Cohen, S., Jung, C., Hu, L., Mok, S.I., Shah, A., Savner, E.M., et al. (2010). Loss of inhibitory interneurons in the dorsal spinal cord and elevated itch in Blhbl5 mutant mice. *Neuron* 65, 886–898.
- Rossi, J., Balthasar, N., Olson, D., Scott, M., Berglund, E., Lee, C.E., Choi, M.J., Lauzon, D., Lowell, B.B., and Elmquist, J.K. (2011). Melanocortin-4

- receptors expressed by cholinergic neurons regulate energy balance and glucose homeostasis. *Cell Metab.* 73, 195–204.
- Ruel, J., Emery, S., Nouvian, R., Bersot, T., Amilhon, B., Van Rybroek, J.M., Rebillard, G., Lenoir, M., Eybalin, M., Delprat, B., et al. (2008). Impairment of SLC17A8 encoding vesicular glutamate transporter-3, VGLUT3, underlies nonsyndromic deafness DFNA25 and inner hair cell dysfunction in null mice. *Am. J. Hum. Genet.* 83, 278–292.
- Ryugo, D.K. (2008). Projections of low spontaneous rate, high threshold auditory nerve fibers to the small cell cap of the cochlear nucleus in cats. *Neuroscience* 154, 114–126.
- Sachs, M.B., and Abbas, P.J. (1974). Rate versus level functions for auditory-nerve fibers in cats: tone-burst stimuli. *J. Acoust. Soc. Am.* 56, 1835–1847.
- Satija, R. 2018. Seurat - guided clustering tutorial. <https://satijalab.org/seurat/pbmc3kTutorial.html>.
- Satija, R., Farrell, J.A., Gennert, D., Schier, A.F., and Regev, A. (2015). Spatial reconstruction of single-cell gene expression data. *Nat. Biotechnol.* 33, 495–502.
- Schmiedt, R.A. (1989). Spontaneous rates, thresholds and tuning of auditory-nerve fibers in the gerbil: comparisons to cat data. *Hear. Res.* 42, 23–35.
- Schmiedt, R.A., Mills, J.H., and Boettcher, F.A. (1996). Age-related loss of activity of auditory-nerve fibers. *J. Neurophysiol.* 76, 2799–2803.
- Seal, R.P., Akil, O., Yi, E., Weber, C.M., Grant, L., Yoo, J., Clause, A., Kandler, K., Noebels, J.L., Glowatzki, E., et al. (2008). Sensorineural deafness and seizures in mice lacking vesicular glutamate transporter 3. *Neuron* 57, 263–275.
- Sergeyenko, Y., Lall, K., Liberman, M.C., and Kujawa, S.G. (2013). Age-related cochlear synaptopathy: an early-onset contributor to auditory functional decline. *J. Neurosci.* 33, 13686–13694.
- Shnerson, A., and Pujol, R. (1981). Age-related changes in the C57BL/6J mouse cochlea. I. Physiological findings. *Brain Res.* 254, 65–75.
- Spoendlin, H. (1969). Innervation patterns in the organ of corti of the cat. *Acta Otolaryngol.* 67, 239–254.
- Spoendlin, H. (1979). Sensory neural organization of the cochlea. *J. Laryngol. Otol.* 93, 853–877.
- Sun, S., Babola, T., Pregernig, G., So, K., Nguyen, M., Su, M., Palermo, A., Berghes, D.E., Burns, J.C., and Müller, U. (2018). Hair cell mechanotransduction regulates spontaneous activity and spiral ganglion subtype specification in the auditory system. *Cell* 174. Published online August 2, 2018. <https://doi.org/10.1016/j.cell.2018.07.008>.
- Taberner, A.M., and Liberman, M.C. (2005). Response properties of single auditory nerve fibers in the mouse. *J. Neurophysiol.* 93, 557–569.
- Tekinay, A.B.A., Nong, Y., Miwa, J.M., Lieberam, I., Ibanez-Tallon, I., Greengard, P., and Heintz, N. (2009). A role for LYNX2 in anxiety-related behavior. *Proc. Natl. Acad. Sci. USA* 106, 4477–4482.
- Tsuji, J., and Liberman, M.C. (1997). Intracellular labeling of auditory nerve fibers in guinea pig: central and peripheral projections. *J. Comp. Neurol.* 381, 188–202.
- van der Maaten, L., and Hinton, G. (2008). Visualizing data using t-SNE. *J. Mach. Learn. Res.* 9, 2579–2605.
- Weisz, C., Glowatzki, E., and Fuchs, P. (2009). The postsynaptic function of type II cochlear afferents. *Nature* 461, 1126–1129.
- Weisz, C.J.C., Glowatzki, E., and Fuchs, P.A. (2014). Excitability of type II cochlear afferents. *J. Neurosci.* 34, 2365–2373.
- Wichmann, C., and Moser, T. (2015). Relating structure and function of inner hair cell ribbon synapses. *Cell Tissue Res.* 361, 95–114.
- Winter, I.M., Robertson, D., and Yates, G.K. (1990). Diversity of characteristic frequency rate-intensity functions in guinea pig auditory nerve fibres. *Hear. Res.* 45, 191–202.
- Yin, Y., Liberman, L.D., Maison, S.F., and Liberman, M.C. (2014). Olivocochlear innervation maintains the normal modiolar-pillar and habenular-cuticular gradients in cochlear synaptic morphology. *J. Assoc. Res. Otolaryngol.* 15, 571–583.
- Yoshikawa, M., Senzaki, K., Yokomizo, T., Takahashi, S., Ozaki, S., and Shiga, T. (2007). Runx1 selectively regulates cell fate specification and axonal projections of dorsal root ganglion neurons. *Dev. Biol.* 303, 663–674.
- Yu, W.M., Appler, J.M., Kim, Y.H., Nishitani, A.M., Holt, J.R., and Goodrich, L.V. (2013). A Gata3-Mafb transcriptional network directs post-synaptic differentiation in synapses specialized for hearing. *eLife* 2, e01341.
- Zou, M., Li, S., Klein, W.H., and Xiang, M. (2012). Brn3a/Pou4f1 regulates dorsal root ganglion sensory neuron specification and axonal projection into the spinal cord. *Dev. Biol.* 364, 114–127.

## STAR★METHODS

## KEY RESOURCES TABLE

REAGENT or RESOURCE	SOURCE	IDENTIFIER
<b>Antibodies</b>		
Mouse anti-CtBP2 IgG1	BD Biosciences	Cat#612044; RRID:AB_399431
Mouse anti-Glutamate Receptor 2, extracellular, clone 6C4 IgG2a	EMD Millipore	Cat#MAB397; RRID:AB_11212990
Rabbit anti-Myosin-VIIa IgG	Proteus Biosciences	Cat#25-6790; RRID:AB_2314838
Chick anti-Neurofilament H IgY	EMD Millipore	Cat#AB5539; RRID:AB_177520
Rabbit anti-dsRed	Clontech Laboratories	Cat#632496; RRID:AB_10013483
Goat anti-Calretinin	EMD Millipore	Cat#AB1550; RRID:AB_90764
Mouse anti-Brn3a, POU-domain protein, clone 5A3.2	EMD Millipore	Cat#MAB1585; RRID:AB_94166
Goat anti-Parvalbumin	Swant	Cat#PVG213; RRID: AB_2650496
<b>Critical Commercial Assays</b>		
RNAscope Probe Mm-Calb2-C3	Advanced Cell Diagnostics	Cat#313641-C3
RNAscope Probe Mm-Pou4f1-C2	Advanced Cell Diagnostics	Cat#414671-C2
RNAscope Probe Mm-Th	Advanced Cell Diagnostics	Cat#317621
RNAscope Probe Mm-Tsc22d3	Advanced Cell Diagnostics	Cat#448341
RNAscope Probe Mm-Epha4	Advanced Cell Diagnostics	Cat#419081
RNAscope Probe Mm-Hcrtr2	Advanced Cell Diagnostics	Cat#460881
RNAscope Probe Mm-Kcns3	Advanced Cell Diagnostics	Cat#467371
RNAscope Probe Mm-Lypd1	Advanced Cell Diagnostics	Cat#318361
RNAscope Multiplex Fluorescent Reagent Kit	Advanced Cell Diagnostics	Cat#320850
Papain	Worthington	Cat#LK003178
Ovomucoid albumin inhibitor	Worthington	Cat#LK003182
DNase	Worthington	Cat#LK003172
PrimeScript Reverse Transcriptase	Takara	Cat#2680A
iTaq Universal SYBR Green Supermix	Biorad	Cat#1725121
Smart-seq2 reagents	Picelli et al., 2013	N/A
<b>Experimental Models: Organisms/Strains</b>		
Mouse: <i>Bhlhb5</i> <sup>Cre</sup>	Michael Greenberg; Ross et al., 2010	<i>Bhlhe22</i> <sup>tm3.1(cre)Meg</sup> MGI:4440745
Mouse: <i>Ai14</i>	The Jackson Laboratory; Madisen et al., 2010	<i>Gt(ROSA)26Sor</i> <sup>tm1(CAG-tdTomato)Hze</sup> MGI:3809524
Mouse: <i>Vglut3</i> <sup>-/-</sup>	The Jackson Laboratory; Seal et al., 2008	<i>Slc17a8</i> <sup>tm1Edw</sup> MGI:3777601
Mouse: <i>Mafb</i> <sup>CreERT2</sup>	Filippo Rijli; Di Meglio et al., 2013	<i>Tg(Mafb-cre/ERT2)#Fmr</i> MGI:5474190
Mouse: <i>Ai9</i>	The Jackson Laboratory; Madisen et al., 2010	<i>t(ROSA)26Sortm9(CAG-tdTomato)Hze</i> MGI:3809523
Mouse: <i>Chat</i> <sup>Cre</sup>	The Jackson Laboratory; Rossi et al., 2011	<i>Chat</i> <sup>tm1(cre)Lowl</sup> MGI:3689420

(Continued on next page)

**Continued**

REAGENT or RESOURCE	SOURCE	IDENTIFIER
Mouse: CD1	Charles River	Strain Code: 022
Mouse: CBA/CaJ	The Jackson Laboratory	Stock No.: 000654
Oligonucleotides		
Oligo-dT <sub>30</sub> VN for Smart-seq2: AGACGTGTGCTCTCCGATCT(T) <sub>30</sub> VN	Integrated DNA Technologies; <a href="#">Satija et al., 2015</a>	N/A
Template-switching oligo for Smart-seq2: AGACGTGTGCTCTCCGATCTNNNNNnGrGrG	Integrated DNA Technologies; <a href="#">Satija et al., 2015</a>	N/A
ISPCR primer for Smart-seq2: AGACGTGTGCTCTCCGATCT	Integrated DNA Technologies; <a href="#">Satija et al., 2015</a>	N/A
qPCR primer for <i>Mpz</i> Forward: GTCAAGTCCCCAGTAGAA	Integrated DNA Technologies	N/A
Reverse: AGGAGCAAGAGGAAAGCAC		
qPCR primer for <i>Pip</i> Forward: AGCAAAGTCAGCCGCAAAAC	Integrated DNA Technologies	N/A
Reverse: CCAGGGAAAGCAAAGGGGG		
Software and Algorithms		
Imaris	BitPlane <a href="http://www.bitplane.com/imaris/imaris">http://www.bitplane.com/imaris/imaris</a>	RRID:SCR_007370
ImageJ	NIH <a href="https://imagej.nih.gov/ij/">https://imagej.nih.gov/ij/</a>	RRID:SCR_003070
AMIRA 3D Analysis	FEI <a href="https://www.fei.com/software/amira-3d-for-life-sciences/">https://www.fei.com/software/amira-3d-for-life-sciences/</a>	Version 6.4; RRID:SCR_014305
R Project for Statistical Computing	<a href="https://cran.r-project.org/">https://cran.r-project.org/</a>	Version 3.3.2; RRID:SCR_001905
Seurat	<a href="https://github.com/satijalab/seurat">https://github.com/satijalab/seurat</a>	Version 1.4.0.12; RRID:SCR_007322
t-distributed Stochastic Neighbor Embedding	Van Der Maaten and Hinton, 2008 <a href="https://lvdmaaten.github.io/tsne/">https://lvdmaaten.github.io/tsne/</a>	RRID:SCR_016342
edgeR	<a href="https://bioconductor.org/packages/release/bioc/html/edgeR.html">https://bioconductor.org/packages/release/bioc/html/edgeR.html</a>	Version 3.19.3; RRID:SCR_012802
randomForest	<a href="https://cran.r-project.org/web/packages/randomForest/index.html">https://cran.r-project.org/web/packages/randomForest/index.html</a>	Version 4.6-12; RRID:SCR_015718
prcomp	Stats R package; <a href="http://stat.ethz.ch/R-manual/R-devel/library/stats/html/prcomp.html">http://stat.ethz.ch/R-manual/R-devel/library/stats/html/prcomp.html</a>	Version 4.3.4.4; RRID:SCR_014676
featureCounts	Subread package; <a href="http://subread.sourceforge.net">http://subread.sourceforge.net</a>	Version 1.4.6-p3; RRID:SCR_012919
STAR	<a href="https://github.com/alexdobin/STAR">https://github.com/alexdobin/STAR</a>	Version 2.4.0j; RRID:SCR_015899
Other		
Raw and processed RNA-sequencing data	NCBI Gene Expression Omnibus	GSE114997

**CONTACT FOR REAGENT AND RESOURCE SHARING**

Further information and requests for resources and reagents should be directed to and will be fulfilled by the Lead Contact, Lisa V. Goodrich ([lisa\\_goodrich@hms.harvard.edu](mailto:lisa_goodrich@hms.harvard.edu)).

## EXPERIMENTAL MODEL AND SUBJECT DETAILS

### Mice

All animal experiments were approved by the Institutional Animal Care and Use Committee (IACUC) of Harvard Medical School and the Massachusetts Eye and Ear Infirmary as appropriate, and conducted following ethical guidelines described in the *US National Institutes of Health Guide for the Care and Use of Laboratory Animals*. The following mouse lines were used:

1. Mice harboring the transgenes *Bhlhb5*<sup>Cre/+</sup>; *Ai14/+* and *Bhlhb5*<sup>Cre/+</sup>; *Ai14/+*; *Vglut3*<sup>-/-</sup> were used for single cell RNA-seq experiments. Both males and females aged P25 to P27 were used and all mice were of mixed C57BL/6J and CD1 backgrounds. The *Bhlhb5*<sup>Cre</sup> line, in which the coding sequence at the *Bhlhb2* locus is replaced with that for Cre recombinase, was kindly provided by Dr. Michael Greenberg (Harvard Medical School, Boston, USA) (Ross et al., 2010). The *Vglut3*<sup>-/-</sup> line was obtained from The Jackson Laboratory (B6;129S2-*Slc17a8*<sup>tm1Edw</sup>/J; Stock No: 016931) and contains an EGFP sequence knocked into exon 2 of the *Slc17a8* locus, which abolishes *Vglut3* expression in these mice (Seal et al., 2008). The *Ai14* line was obtained from The Jackson Laboratory (Madisen et al., 2010). In addition, the following lines were used to study the developmental emergence of subtype identities by RNAscope: 1) *Bhlhb5*<sup>Cre/+</sup>; *Ai14/+*, 2) *Vglut3*<sup>+/-</sup> and 3) *Vglut3*<sup>-/-</sup>. All mice used for data collection were born and reared in a barrier animal facility at Harvard Medical School, Boston, USA.
2. Mice harboring the transgenes *Mafb*<sup>CreERT2/+</sup>; *Ai9/+* were used for immunohistochemistry and neuroanatomical tracing. *Mafb*<sup>CreERT2</sup>, a bacterial artificial chromosome (BAC) transgenic line (MGI: 5474190), was kindly provided by Dr. Filippo Rijli (Friedrich Miescher Institute for Biomedical Research, Basel, Switzerland) (Di Meglio et al., 2013). The *Ai9* line was obtained from The Jackson Laboratory (Madisen et al., 2010). All mice used for data collection were of mixed C57BL/6J and CD1 background and born and reared in a barrier animal facility at Harvard Medical School, Boston, USA.
3. Cochleae of *Chat*<sup>Cre/+</sup>; *Ai14/+* mice were used for immunohistochemistry. Both the *Chat*<sup>Cre</sup> (Rossi et al., 2011) and *Ai14* (Madisen et al., 2010) lines were obtained from The Jackson Laboratory. All mice used for data collection were of mixed C57BL/6J and CD1 background and born and reared in a barrier animal facility at Harvard Medical School, Boston, USA.
4. Animals used for age-related loss of spiral ganglion neurons were of CBA/CaJ background and born and reared in a barrier animal facility at the Massachusetts Eye and Ear Infirmary, Boston, USA. The acoustic environment of the facility has been described previously (Sergeyenko et al., 2013). Mice of both sexes were used at all time points.
5. CD1 mice (Charles River, Stock No. 022) of both sexes and aged P25-P27 were used for validation of gene expression by RNAscope. Mice were housed 0 to 7 days after purchase in a barrier animal facility at Harvard Medical School, Boston, USA before tissue collection.

## METHOD DETAILS

### Single cell RNA-sequencing

High throughput scRNA-seq approaches such as Dropseq and Indrop offer ease of profiling and classifying cells but at the cost of low information content per cell. Since our goal was to both classify neurons and gain a deep understanding of the transcriptomic basis of neuronal identities, we chose to combine manual neuron collection with the Smart-seq2 approach that offers a high rate of transcript sampling per cell and sequencing of full-length transcripts. Our workflow is described in detail below.

### Collection of single neurons

Cochleae of P25 - P27 mice (Genotypes: *Bhlhb5*<sup>Cre/+</sup>; *Ai14/+* and *Bhlhb5*<sup>Cre/+</sup>; *Ai14/+*; *Vglut3*<sup>-/-</sup>) were dissected out of the inner ear. Each cochlea was further dissected to isolate the most apical, middle, or basal turn and subsequent processing of each turn was done separately to permit tracking of each neuron's origin along the tonotopic axis. Pieces of the cochlea were then digested first with collagenase (25 min at 37°C) then 40 U/ml papain (25 min at 37°C) (Worthington, LK003150) before passing through a discontinuous density gradient of ovomucoid protease inhibitor (Worthington, LK003182). The crude dissociation extract was passed through a 40 µm cell strainer (Corning, 352340) and placed in a Petri dish with a glass bottom microwell (Cellvis, D60-14-1N) for manual collection. Neurons expressing tdTomato were identified under a dissecting microscope (Olympus, MVX10) and a small number of them (typically < 100) were gently transferred to a clean droplet of transfer buffer (10% ovomucoid protease inhibitor in 1x EBSS (Invitrogen, 14155-063)) using a glass micropipette attached to suction tubing. To get rid of debris and non-neuronal cells that accompany tdTomato<sup>+</sup> neurons during the transfer, cells were rinsed five times by aspirating and expelling them sequentially into a series of clean transfer buffer droplets on the same Petri dish, taking care to aspirate only tdTomato<sup>+</sup> cells each time. After the final rinse, a neuron-enriched pool with no visible tdTomato-negative cells or floating debris was obtained. Neurons were then placed one-by-one at the bottom of individual 0.2 mL tubes (Axygen, 321-10-061) using a fine glass micropipette (typically 40 µm internal diameter at the tip) attached to suction tubing. To avoid contamination resulting from cells that lyse during transfer, glass micropipettes and tubes were never reused after failed transfers. A typical transfer resulted in 1-2 µl of transfer buffer in the tube, most of which was aspirated out of the tube, leaving ~0.3 µL behind. To ensure collection of a healthy single neuron per tube, maintenance of strong red fluorescence, lack of cell shrinkage, and absence of other neurons in the same tube were visually verified for every sample under high magnification. Any sample that did not meet all three of these criteria was discarded. Cells were

immediately frozen after transfer and stored at  $-80^{\circ}\text{C}$  for further processing. All cells were collected between 1 PM and 8 PM. Collection of single cells started  $\sim 75$  min after sacrificing the animal and ended after 2 hr. Time elapsed between euthanization of the animal and freezing of cells varied between 90 and 195 min. Both ears of every mouse and mice of both sexes were used.

#### cDNA and library preparation

cDNA libraries were made by the Smart-seq2 method, essentially as described previously (Picelli et al., 2013) but with the following modifications: 1) ERCC spike-in controls (1  $\mu\text{l}$  at 1:50000 dilution, Ambion, 4456740) were added at the cell lysis step; 2) first-strand synthesis was done using Primescript Reverse Transcriptase (Takara, 2680A); 3) 19 cycles of PCR amplification was done; 4) the following primers were used (Satija et al., 2015):

Oligo-dT<sub>30</sub>VN: 5'-AGACGTGTGCTCTCCGATCT(T)<sub>30</sub>VN-3'  
Template-switching oligo: 5'-AGACGTGTGCTCTCCGATCTNNNNNNrGrGrG-3'  
ISPCR: 5'-AGACGTGTGCTCTCCGATCT-3'

Sample quality and yield were analyzed using the high-sensitivity DNA kit in a bioanalyzer (Agilent).

#### qPCR screening

SGN cell bodies in mice are naturally ensheathed by satellite glia after neonatal stages. We found that a small proportion of SGNs dissociated using the protocol described above lost their associated ensheathing glia, but most retained it. This posed a challenge for obtaining neuron-specific transcriptome due to possible contamination from transcripts derived from satellite glia. Given the low proportion of cells that visibly lacked ensheathing glia under high magnification, we chose to pick tdTomato-positive SGNs without regard to their ensheathment status, and instead enriched for neuron-specific libraries by screening out those containing glia-derived transcripts by qPCR. Specifically, presence of Mpz (F: 5'-GTCAAGTCCCCAGTAGAA-3', R: 5'-AGGAGCAAGAGGAAGCAC-3') and Plp (F: 5'-AGCAAAGTCAGCCGCAAAC-3', R: 5'-CCAGGGAAGCAAAGGGGG -3') were probed and only libraries that were negative for both transcripts were included in the library enrichment step of the Smart-seq2 protocol.

#### Tissue processing for mRNA/protein detection

Cochlear whole mounts and sections were processed as described previously (Yu et al., 2013). The following primary antibodies were used: anti-Calb2 (1:600), anti-Pou4f1 (anti-Brn3a) (1:300), anti-Parvalbumin (1:500), anti-GluA2 (1:500), anti-CtBP2 (1:500), anti-Myo7a (1:1000), anti-dsRed (1:1000), anti-NF-H (1:1000). For immunostaining of Pou4f1, antigen retrieval in 10 mM citrate buffer (pH 6.0) was done for 20 min before commencing with the staining protocol.

For mRNA detection by RNAscope (Advanced Cell Diagnostics), the manufacturer's protocol was used with the exception that at the end of the protocol, tissues were stained overnight with anti-Parvalbumin, followed by incubation in the appropriate secondary for 2 hrs the next day. The following probes were used: Mm-Calb2 (Cat#313641-C3), Mm-Pou4f1 (Cat#414671-C2), Mm-Th (Cat#317621), Mm-Tsc22d3 (Cat#448341), Mm-Epha4 (Cat#419081), Mm-Lypd1 (Cat#318361), Mm-Hcrtr2 (Cat#460881), Mm-Kcns3 (Cat#467371).

## QUANTIFICATION AND STATISTICAL ANALYSIS

#### Sequencing and bioinformatic analysis

Sequencing was done in a NextSeq platform (Illumina) over 2 runs, with similar numbers of samples corresponding to different genetic backgrounds, ages, and cochlear origin mixed across the runs. De-multiplexed raw reads were processed using custom-written UNIX scripts in a shared high-performance computing cluster running CentOS Linux. The following steps and settings were used: 1) low-quality and short reads were trimmed using Trimmomatic (0.33) (PE -phred33 SLIDINGWINDOW:4:20 MINLEN:22 PE -phred33 SLIDINGWINDOW:4:20 MINLEN:22); 2) reads were aligned using STAR to the mouse genome (mm10) to which sequences corresponding to ERCC spike-ins and tdTomato had been appended (-sjdbOverhang 37 \outFilterScoreMinOverLread 0.4 \outFilterMatchNminOverLread 0.4); 3) reads mapped to the mouse transcriptome were counted using the featureCounts program of the Subread package (v1.4.6). Transcriptome-wide counts for all samples were merged into a table, which was then imported into R (v3.3.2). Analyses and visualization of results within the R environment were done using a custom-written script that utilized Seurat (v 1.4.0.12) for dimension reduction, t-SNE, unsupervised clustering and differential expression analyses, edgeR for normalization, and randomForest for supervised classification.

#### Data normalization

Type II SGNs have smaller cell bodies than Type I neurons (Brown, 1987). In addition, heterogeneities in cell size both locally and across the tonotopic axis have been noted (unpublished data; Echteler and Nofsinger, 2000). To account for differences in RNA content arising from cell size heterogeneity, we performed trimmed mean of M-values (TMM) normalization on raw read counts using the edgeR package before importing the expression matrix into Seurat. Cell classification was also conducted without TMM normalization with nearly identical results. No other normalization or transformation was done beside log normalization of counts performed within Seurat. All log-normalized maximum count values for individual genes reported in t-SNE and dot-matrix plots include additional normalization of raw read counts to account for gene length differences. However, these values were used strictly for visual reporting in such plots and not for any other aspect of our analyses.

### Cell filter

Only libraries meeting the following criteria were analyzed: 1) free of glial-markers (i.e., *Mpz*, *Gjc3*, *Mbp* all  $\leq 1$ ); 2) total reads  $> 750000$ ; 3) proportion of ERCC spike-in transcripts  $< 20\%$ ; 4) proportion of transcripts from mitochondrial genome  $< 10\%$ ; 4) genes detected  $\geq 4000$ .

### Dimension reduction

Principal component analysis (PCA) was done using variable genes defined as described in the Seurat manual ([Satija, 2018](#)). Genes expressed ( $> 1$  count) in fewer cells than a set cutoff (i.e., cubed root of no. of cells in the quality-filtered dataset) were deemed to be ultra-sparse and hence omitted from the variable gene list used for PCA. In addition, all exogenous transcripts (ERCC spike-in and tdTomato) were removed. Between 8 and 20 top PCs were then selected to generate 2-dimensional embeddings for data visualization using t-SNE for various subsets. The set of PCs used always included those contained within the first elbow in a scree plot as well as those deemed statistically significant in Jack Straw plots and explained 60%–70% variance in the dataset. Because t-SNE outcome can vary slightly from run to run even under the same settings, t-SNE coordinates generated in initial runs were saved and re-used in subsequent runs for consistency in visualization.

### Unsupervised clustering

scRNA-seq profiles were classified via an unsupervised graph-based clustering algorithm implemented in Seurat (v1.4.0.12) that embeds cells in a K-nearest neighbor (KNN) graph and determines clusters by iteratively grouping cells while optimizing the standard modularity function ([Butler et al., 2018](#); [Satija et al., 2015](#)). In this approach, granularity of the clustering is dependent on a user-specified ‘resolution’ parameter within the *FindCluster* function in Seurat. To ensure unbiased selection of the appropriate number of clusters for classifying Type I SGNs, clustering was conducted using 46 different values of this parameter, ranging from 0.4 to 1.3 with increments of 0.02. Predictions of 3 clusters were obtained across 42 out of those 46 runs (91%) ([Figure S1B](#)), with 97% of cells being assigned the same identity across such runs ([Figure S1C](#)). This led to the conclusion that the major structure in the single-cell transcriptomic data were captured by classification into 3 clusters, and by extension, reflected the existence of 3 distinct neuronal subtypes. Additionally, hierarchical clustering based on Ward’s method and Euclidean distances was conducted using the *hclust* package in R. In both approaches, only highly variable genes (as described above) were used.

### Training an ensemble learning-based classifier

Consistent with previous reports, we observed that deriving consistent cell type classification became progressively harder with decreasing cell number. To confirm that identifying subtypes among neurons from *Vglut3*<sup>-/-</sup> mice was not affected by sample size, we implemented an ensemble learning method to derive an independent classification. The same 3 subtypes identified across all Type I SGNs ( $n = 179$ ) in our data could be identified even when we analyzed SGNs from the middle turn alone ( $n = 88$ ). Therefore, we employed ensemble learning to generate a classifier trained on just the middle turn neurons using the *randomForest* package in R. The training set consisted of 44 randomly selected neurons (15, 18, 11 of A, B, C subtypes, respectively). We reasoned that differentially expressed genes must be detectable broadly within a cluster for it to be informative for classifying unknown cells, so only genes expressed in  $> 50\%$  of cells in the cluster they are markers for and  $< 50\%$  in the rest were selected. This resulted in a  $44 \times 233$  cell-by-gene matrix, which was used as the training dataset. To assess the classifier’s performance, we used it to predict classes for all wild-type cells not part of the training set, which comprised the test set and included 44, 50, and 41 cells from the middle, apex, and base, respectively. The results were compared against classification produced by graph-based clustering implemented in Seurat ([Figures S7E–G](#)). Training parameters were tuned until the median out-of-bag error rate reached zero and performance in the test set peaked (99%) across  $> 10000$  combinations of the *mtry*, *nodesize* and *ntree* parameters. The following settings were picked: *mtry* = 3, *nodesize* = 1, *ntree* = 1000.

### Image acquisition and analysis

All RNAscope images were acquired at Nyquist settings using a point-scanning confocal microscope (Leica SP8, 63x oil-immersion objective) equipped with hybrid detectors. Image stacks were then analyzed semi-automatically using Imaris (Bitplane, UK). Briefly, cell volumes were segmented using either anti-Parvalbumin stain or anti-dsRed stain (in animals expressing the tdTomato transgene in SGNs). Any cell clipped along the XYZ axes was removed before automatic detection of RNAscope puncta. Parameters for both cell segmentation and puncta detection were set after visually guided search for optimal parameters. In a subset of images (corresponding to data presented in [Figure 5](#) for the 108-wks timepoint) autofluorescent aggregates, which appeared across all channels, interfered with automatic detection of RNAscope puncta. Hence, a Gaussian filter was applied to get rid of such aggregates in channels containing RNAscope signal ([Figure S6A–B](#)). To account for variability in signal:noise ratio across experimental conditions, puncta counts for cells from each image were rescaled to fit max and min values across all cells within each biological group. Cells with puncta count above 10% of the maximum value were considered positive for the marker.

Confocal images of cochlear wholemounts were acquired using the same hardware as above. Images were taken as a  $1024 \times 1024$  pixel raster at 63x (2x digital zoom) and a Z-sampling rate of  $0.308 \mu\text{m}$ . Image stacks were analyzed using Amira (FEI, USA). Volumes of individual pre-synaptic ribbons were computed using Amira’s 3D rendering and masking functions. Briefly, each pre-synaptic ribbon was reconstructed by a 3D ‘isosurface’ which surrounded all the pixels that defined the ribbon. The volume of the isosurface defined the volume of the pre-synaptic ribbon. Differences in sample preparations were normalized by dividing each isosurface by the median isosurface size in a given Z stack. The spatial segregation of individually labeled Type I SGN fibers along the basolateral surface of the inner hair cell was analyzed by generating an isosurface around both the afferent fiber and the target pre-synaptic

puncta. The YZ coordinates of the pre-synaptic ribbon and adjacent afferent terminal were remapped onto an XY plane and assessed. A line bisecting the inner hair cell nucleus and cuticular/basolateral axis defined the 0 position of the pre-synaptic ribbons along the modiolar/pillar axis.

Optical sections of the OSL bundle were taken 50  $\mu\text{m}$  away from the base of the IHCs in Amira (FEI, USA) and all subsequent analyses involving fluorescence intensity measurements were done using ImageJ (1.49v). To analyze CALB2 levels in SGN fibers in the OSL, regions of interest (ROI) were drawn around SGN fibers positive for NF-H in optical cross-sections of confocal Z stacks. Mean fluorescence intensity values for CALB2 were then calculated for all ROIs and normalized to the highest value within an image. Somatic CALB2 fluorescence intensity was quantified in *Mafb*<sup>CreERT2</sup>;Ai9 animals, which exhibit sparse labeling of SGN cell bodies with the tdTomato reporter. ROIs were drawn around tdTomato<sup>+</sup> SGN cell bodies and fluorescence intensity values for CALB2 across all ROIs within an image were normalized to the highest mean fluorescence value in the same image.

#### **Clustering of RNAscope-based expression data**

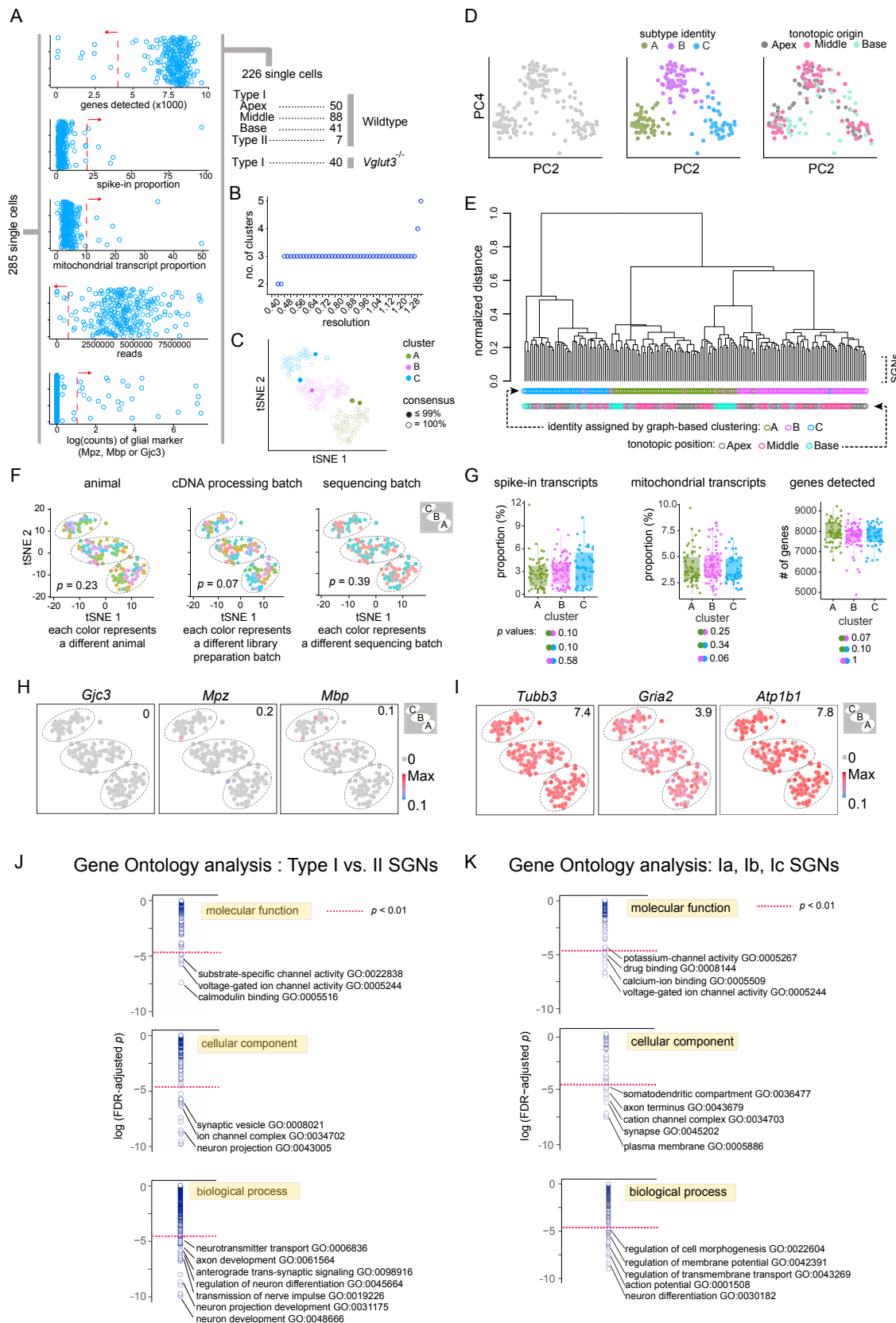
An unsupervised machine learning algorithm (K-means clustering) was utilized to group the CALB2 OSL fluorescence intensity data ([Figures S5C and S5D](#)) into a specified number of clusters. The number of clusters ( $k$ ) was determined based on an elbow plot (sum of squared errors, SSE versus  $k$  clusters) and chosen at the point where the slope approached zero. A total of 3 clusters were found to be appropriate for the CALB2 OSL dataset. Cluster boundaries defined by K-means clustering was used to set the fluorescence intensity cut-offs for ‘low’, ‘medium’, and ‘high’ CALB2 groups ([Figure S5D](#)). K-means clustering was also performed on the RNAscope-based *Lypd1/Calb2* expression data presented in [Figure 5](#). Elbow plots utilized for each dataset are shown in [Figures S6D and S6E](#). All statistical analyses of *in situ* expression data and immunostaining data in [Figures 4 and 5](#) were done in GraphPad Prism 6.0. Analyses of such data in all other figures were done in R.

#### **DATA AND SOFTWARE AVAILABILITY**

The accession number for the data reported in this paper is GEO: GSE114997 ([Edgar et al., 2002](#)). Gene expression data are also viewable in browsable graphical format at <http://goodrich.med.harvard.edu/resources.html>.

# Supplemental Figures

Cell



(legend on next page)

---

**Figure S1. Quality Control Metrics and Gene Ontology Results, Related to Figures 1 and 2**

(A) Scatterplots showing technical and biological criteria used to filter cells before analysis. Red dotted lines indicate cutoff value and red arrows indicate direction of exclusion.

(B) Setting the resolution parameter to values between 0.40 and 1.30 for graph-based clustering in Seurat yielded 2 to 5 clusters, with 42 out of 46 values (91%) predicting 3 clusters.

(C) Agreement with regard to cell identity among all variations of the resolution parameter that yielded 3 clusters. For each cell, a consensus score was calculated as the percentage of times the same identity was assigned to it across clustering runs that varied only in terms of resolution. Consensus was 100% for 174 out of 179 cells (97%).

(D) Projection of SGN transcriptomes onto PCA space (PC2 versus PC4) reveals groups that correspond closely with those identified by graph-based clustering. Each group in the PCA plot contains SGNs from all tonotopic regions.

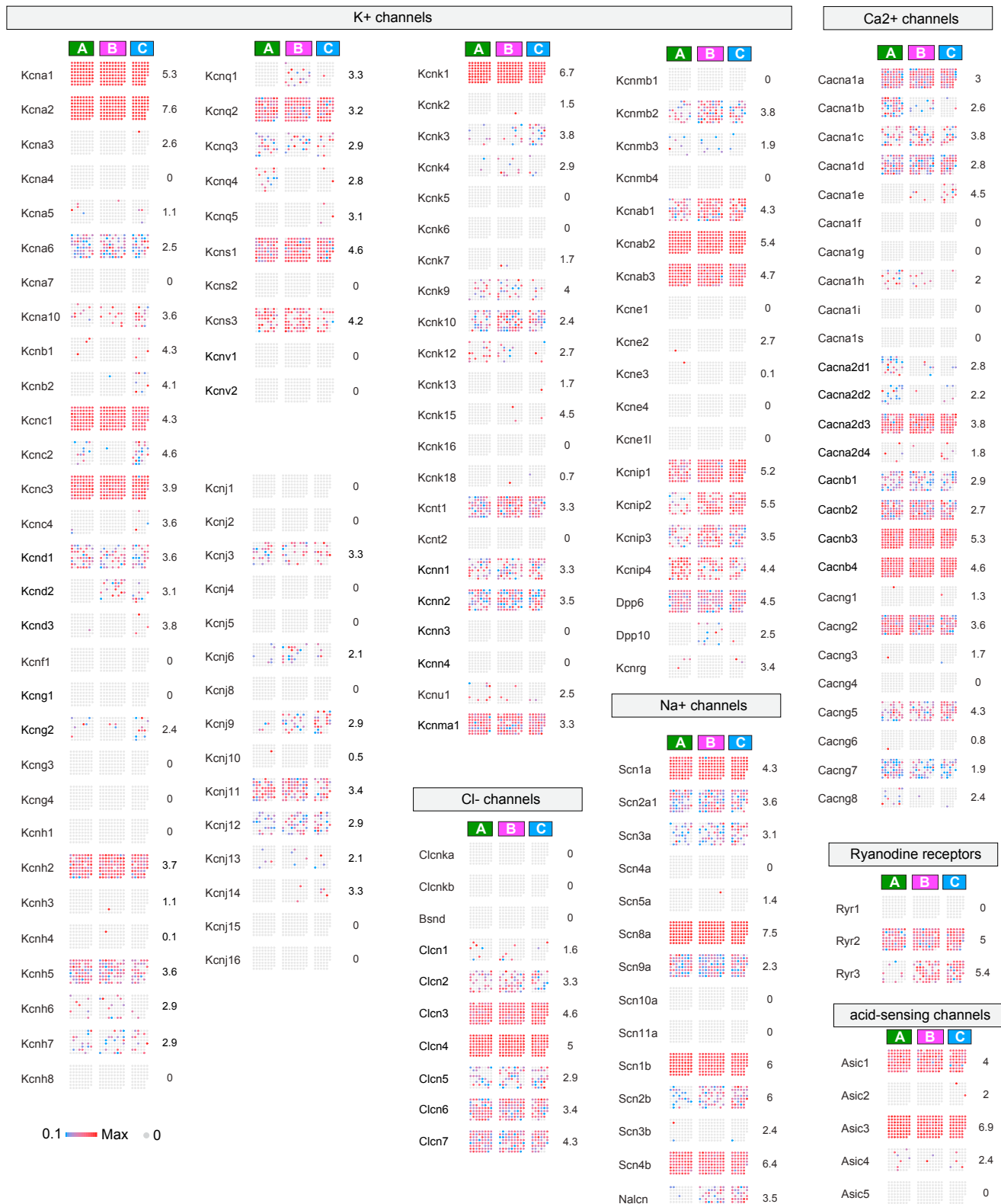
(E) Results of hierarchical clustering by Ward's method depicted as a dendrogram. The three major branches correspond well with SGN subtype identities predicted by graph-based clustering but not with their tonotopic position.

(F) Segregation of SGNs is not driven by technical variables or experimental factors such as sequencing batch. p values refer to Chi-square test of independence.

(G) There were no significant subtype-specific differences in the detection of spike-in transcripts, mitochondrial transcripts, or number of genes detected. Box plots depict median (horizontal line), 25%–75% quartiles (shaded rectangle), smallest observation  $\geq$  25% quartile-1.5\*interquartile range (lower error bar), largest observation  $\leq$  25% quartile + 1.5\* interquartile range (upper error bar). p values are indicated next to pairs of dots that represent subtypes compared by Tukey's HSD test if the data were normally distributed data and Dunn's test otherwise.

(H and I) Absence of glial gene expression (H) and uniform expression of known pan-neuronal genes (I) across the three Type I SGN clusters. Numbers in upper right corner indicate highest expression (Max) observed for each gene.

(J and K) Graphical representation of results of Gene Ontology analysis of genes expressed differentially between Type I and II SGNs (J) or among Type I SGNs (K). A few examples of statistically significantly enriched categories are named.

**Figure S2. SGN Subtypes Express Unique Cohorts of Genes that Influence Neuronal Physiology, Related to Figure 2**

Dot-matrix plots showing expression of gene families relevant to neuronal physiology. Each dot is a neuron profiled by scRNA-seq and neurons are grouped based on subtype identity assigned by unsupervised clustering. Numbers on the right indicate the highest expression (Max) observed for each gene.

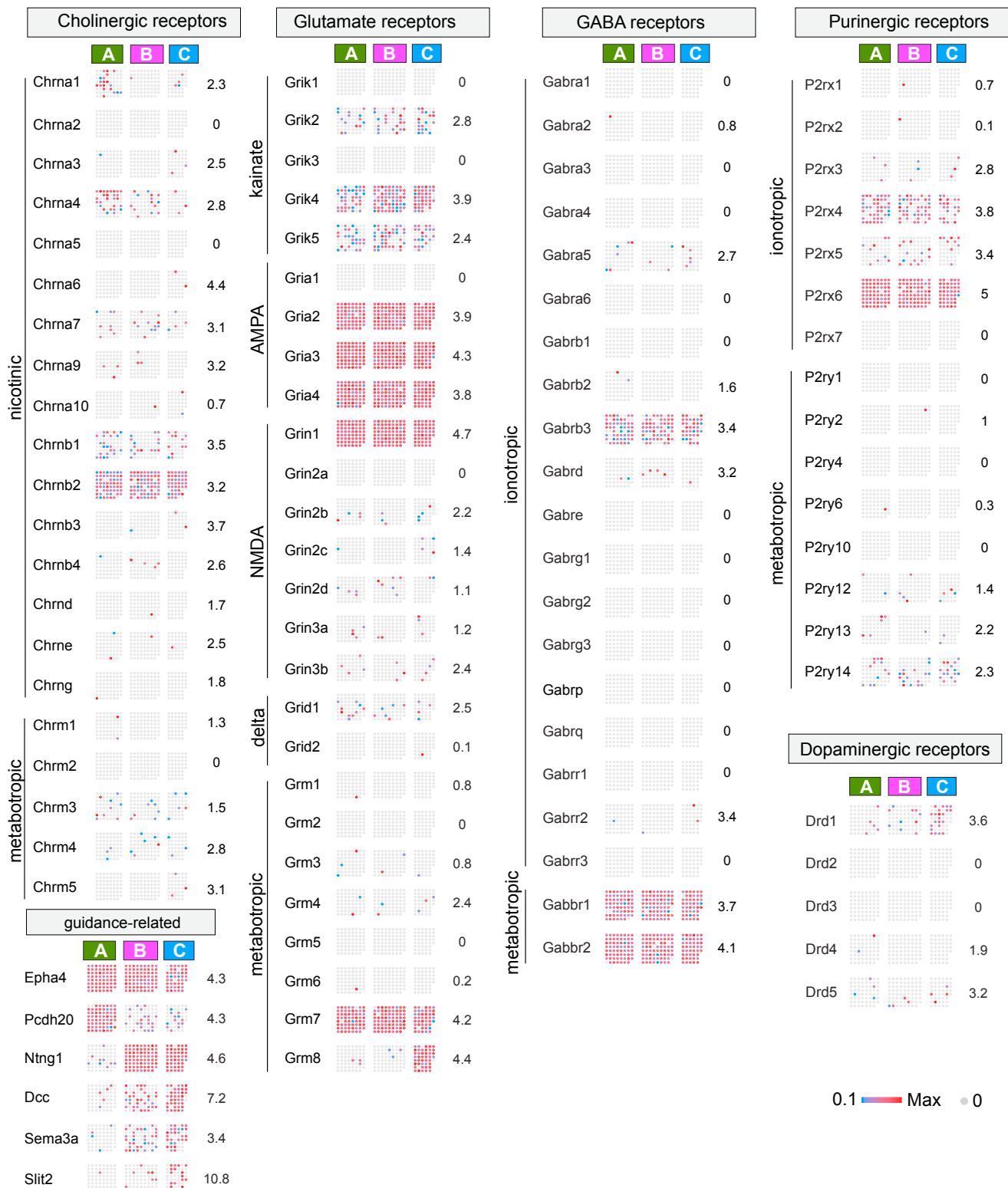
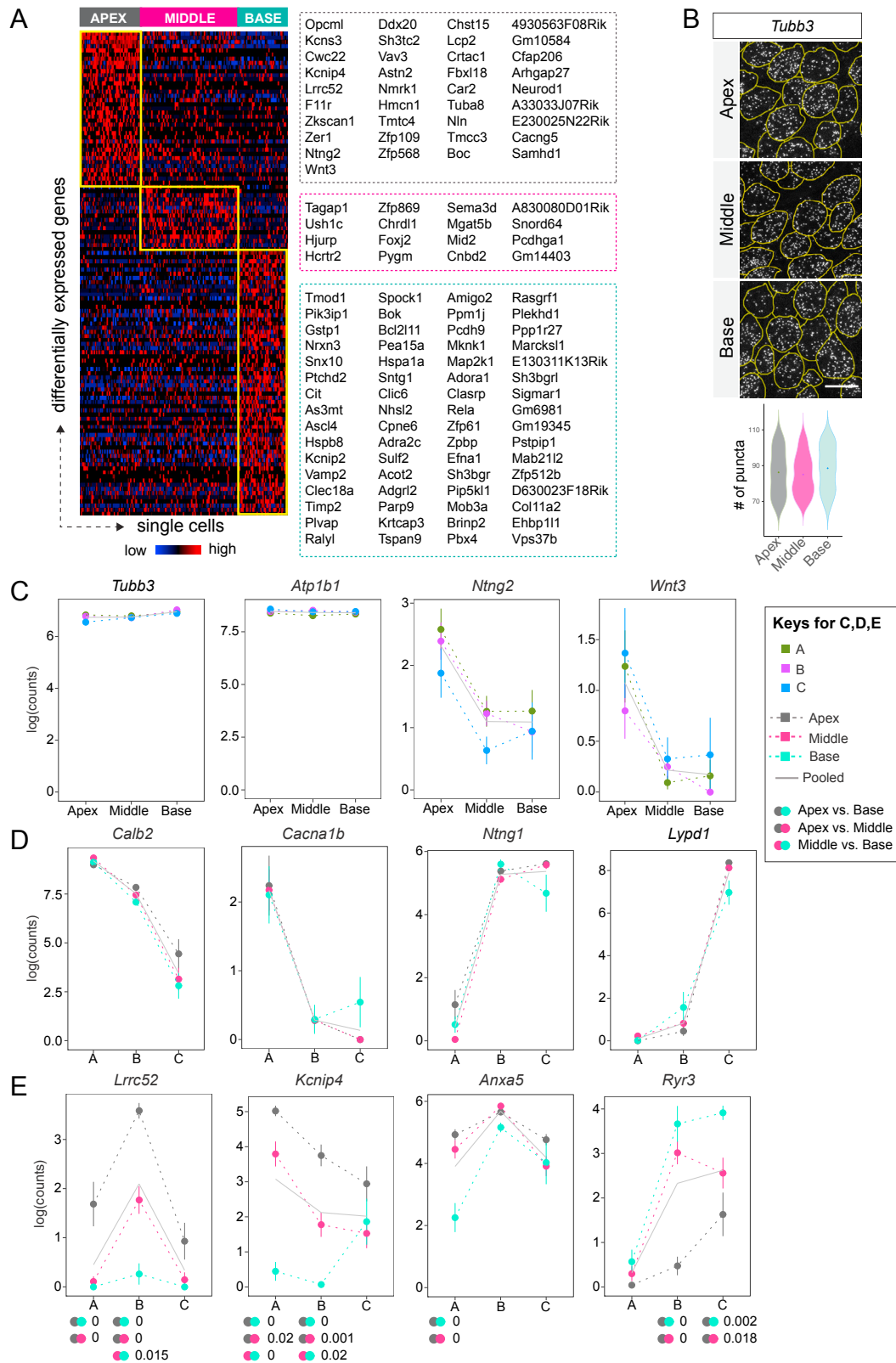


**Figure S3. SGN Subtypes Express Unique Cohorts of Genes that Influence Neurotransmission and Neurite Guidance, Related to Figure 2**  
 Dot-matrix plots showing expression of gene families relevant to neurotransmission and neurite guidance. Each dot is a neuron profiled by scRNA-seq and neurons are grouped based on subtype identity assigned by unsupervised clustering. Numbers on the right indicate the highest expression (Max) observed for each gene.



(legend on next page)

**Figure S4. Tonotopic Differences in Gene Expression across all SGNs and within SGN Subtypes, Related to Figure 3**

(A) Heatmap showing the top 100 most differentially expressed genes across the tonotopic axis. Each column represents a single cell and genes are in rows. Cells were grouped based on tonotopic origin. Panels on the right show examples of genes enriched in the apex (top), middle (middle) and base (bottom).

(B) RNAseq of tissue sections (P25-P27) confirms even expression of the pan-neuronal gene *Tubb3* in the apex, middle, and base of the cochlea, quantified below.

(C) Plots showing expression (mean  $\pm$  SEM) of genes that were invariant across the tonotopic axis for all pooled SGNs (solid lines) and for each subtype (dashed lines: Ia, green; Ib, purple; Ic, blue).

(D) Examples of genes that are robust markers for Ia, Ib, and Ic subtypes across all tonotopic regions. Mean expression levels ( $\pm$  SEM) are shown for Ia (A), Ib (B), and Ic (C) SGNs taken from the apex (gray), middle (red), or base (blue) of the cochlea.

(E) Examples of genes whose cross-subtype variation in expression ( $\pm$  SEM) differs among SGNs from different cochlear regions (apex, gray; middle, red; base, blue). For example, there is significantly lower expression of *Anxa5* in Ia SGNs from the base relative to those from the middle and the apex, but little variation among Ib or Ic SGNs. Pairs of dots indicate p values for comparisons across tonotopic regions by Tukey's HSD test if the data were normally distributed data and Dunn's test otherwise. p values are reported only for statistically significant differences. Scale bars: 10  $\mu$ m (B).

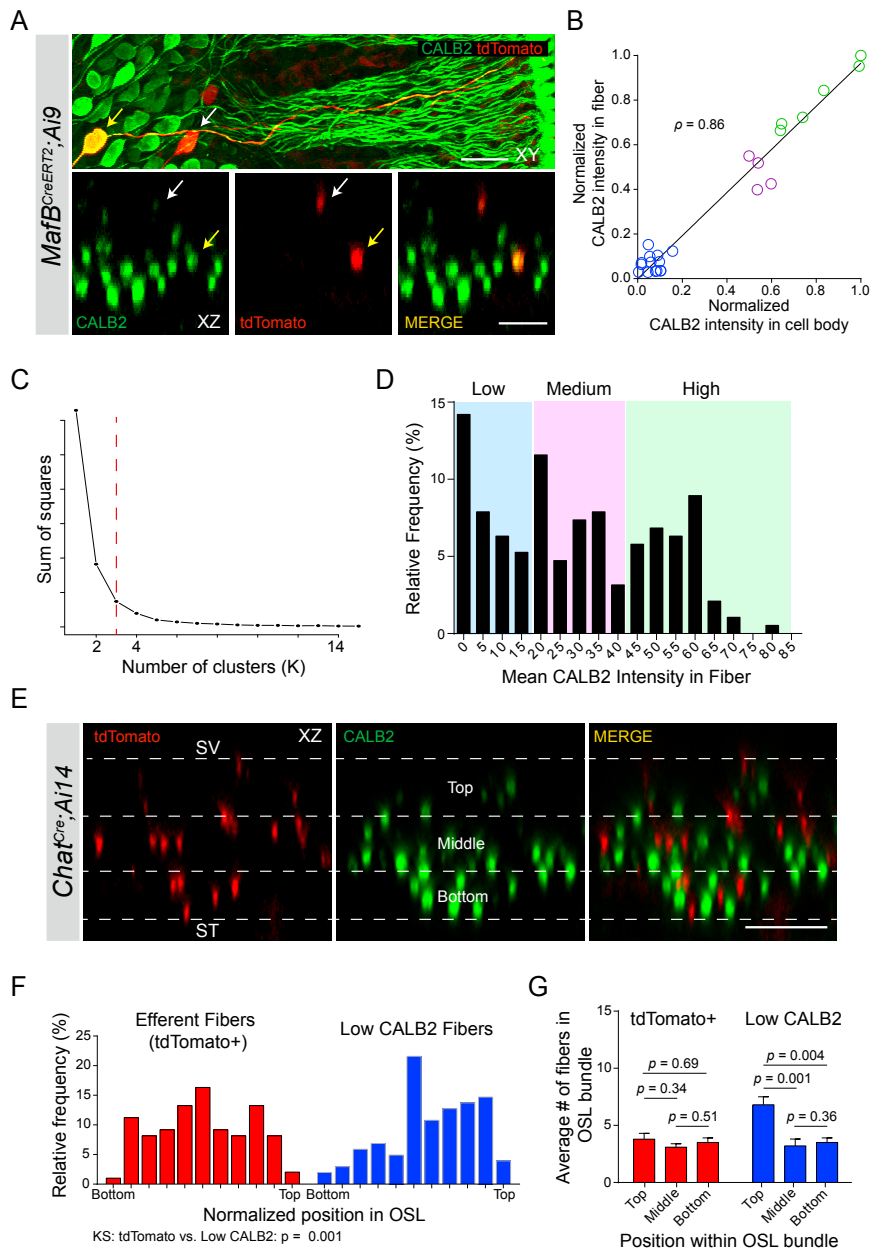


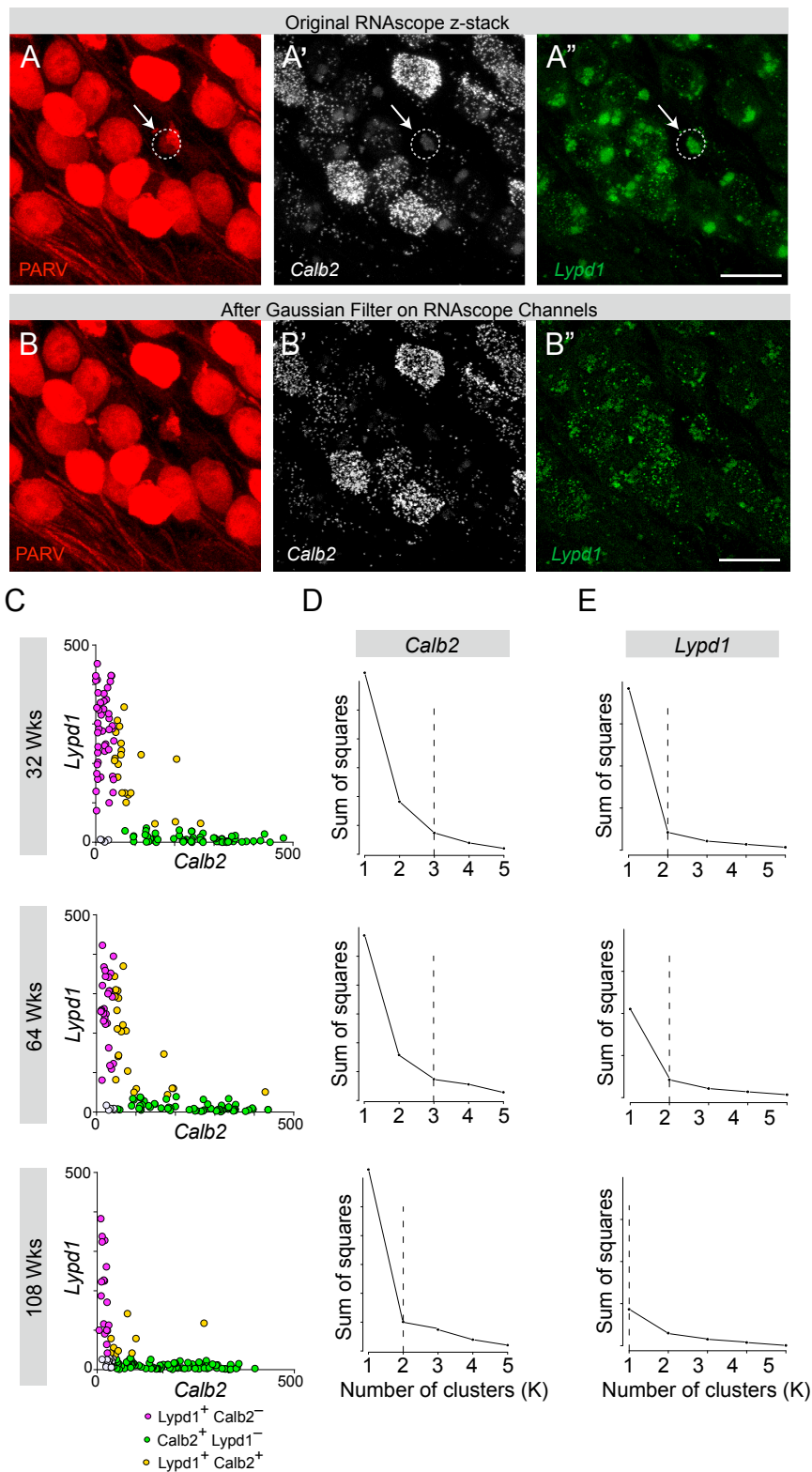
**Figure S5. Operational Definition of SGN Subtypes According to CALB2 Intensity, Related to Figure 4**

(A and B) Wholemount cochlea from *Mafb*<sup>CreERT2</sup>; *Ai9* animals were double-stained for CALB2 (green) and tdTomato (red). Individual tdTomato labeled SGNs could be traced from their cell bodies to the organ of Corti, shown in a top down (XY) view (top). Position in the OSL was assessed in cross-sectional (XZ) views through confocal image stacks (below). CALB2 intensities in cell bodies and processes were correlated for each neuron. Examples of one CALB2<sup>+</sup> SGN (yellow arrow) and one CALB2<sup>low</sup> SGN (white arrow) are shown, with quantification for all analyzed SGNs in B.

(C and D) SGN subtypes were operationally defined based on CALB2 levels. K-means clustering of all measured CALB2 fluorescence intensities in fibers revealed that the expression values are best split into three clusters (red dotted line, C). Fibers were divided into low ( $n = 113$ ), medium ( $n = 78$ ), and high ( $n = 116$ ) CALB2<sup>+</sup> groups as defined by the K-means cluster boundaries, indicated by colored shading in a histogram of all analyzed fibers ( $n = 214$ , 5 animals).

(E) Cross-sectional views (XZ) through the OSL of *Chat*<sup>Cre</sup>; *Ai14* cochlear wholemount preparations immunostained for CALB2 (green) and tdTomato (red). *Chat*<sup>Cre</sup>; *Ai14* labels olivocochlear efferents. Dotted lines indicate the upper limit (toward SV), mid-point and lower limit (toward ST) of the afferent fiber bundle.

(F and G) Histograms show even distribution of efferent fibers (red) but SV-biased distribution of low CALB2 (blue) fibers in the OSL (F). The average number of fibers per region is quantified in G. Error bars in G represent SD. p values indicate results of Kolmogorov-Smirnov (KS) test (F) and results of Tukey's HSD test following one-way ANOVA (G). Scale bars: 10  $\mu$ m.



(legend on next page)

---

**Figure S6. Analysis of *Lypd1* and *Calb2* mRNA Levels in the Aging Mouse Cochlea, Related to Figure 5**

(A and B) In sections of the cochlea at 108 wks, autofluorescent aggregates (arrows) appear in all fluorescent channels (anti-Parvalbumin (PARV), A; *Calb2* RNAscope, A'; *Lypd1* RNAscope, A''). In order to count mRNA puncta reliably, this signal was removed prior to cell segmentation and quantification by applying a Gaussian filter across the fluorescent channels (B–B'').

(C) Scatterplots of *Lypd1* and *Calb2* levels in all SGNs analyzed at 32, 64, and 108 wks ( $n = 5$  animals, 212 cells at 32 weeks,  $n = 5$  animals, 175 cells at 64 weeks,  $n = 5$  animals, 151 cells at 108 weeks, respectively).

(D and E) K-means clustering analysis showed that SGN populations could be sorted into three groups based on *Calb2* levels at 32 wks (top) and 64 wks (middle), but only into 2 groups at 108 wks (bottom), consistent with a loss of Type Ic SGNs. Likewise, whereas two clusters of *Lypd1*+ SGNs can be defined at 32 and 64 wks, only one cluster remains at 108 wks (E). Scale bar: 10  $\mu$ m (A and B).

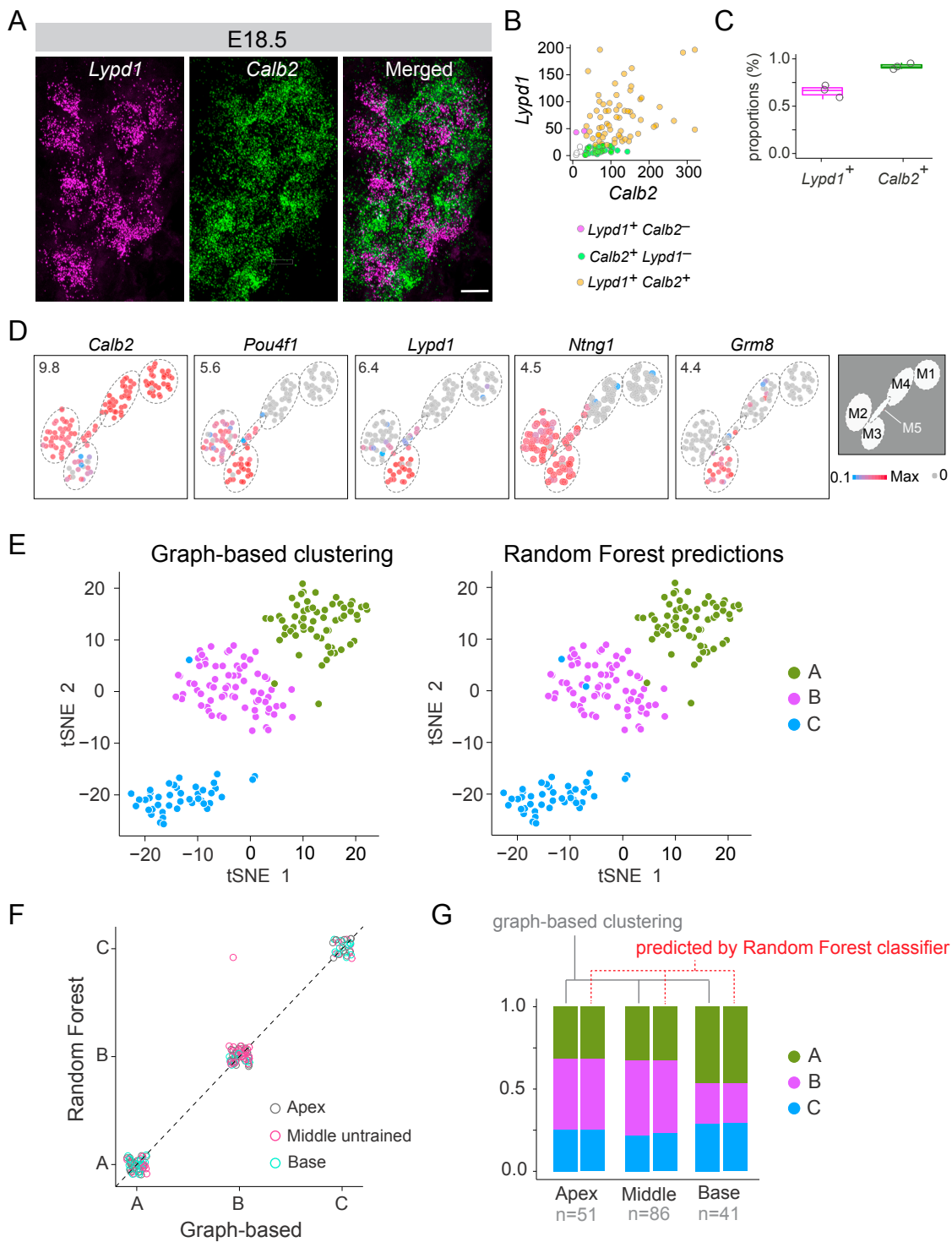


**Figure S7. Marker Expression in Embryonic and *Vglut3*<sup>-/-</sup> Animals, and Comparison of Supervised and Unsupervised Clustering Approaches, Related to Figures 6 and 7**

(A–C) Detection of *Lypd1* (magenta) and *Calb2* (green) transcripts by RNAscope at E18.5 reveals early co-expression in individual SGNs, with *Calb2* expressed broadly but *Lypd1* expressed in a subset, quantified in B. Whereas the vast majority of SGNs express *Calb2*, a smaller proportion express *Lypd1* (C). Box plots in C depict median (horizontal line), 25%–75% quartiles (shaded rectangle), smallest observation  $\geq$  25% quartile-1.5\*interquartile range (lower error bar), largest observation  $\leq$  25% quartile + 1.5\* interquartile range (upper error bar).

(legend continued on next page)

- 
- (D) The level of expression of select subtype-specific markers is overlaid in a t-SNE plot containing both WT (M1-M3 clusters) and *Vglut3*<sup>-/-</sup> cells (M4-M5 clusters). Cluster identities in the key to the right are based on [Figure 7A](#). Numbers on the upper left indicate the highest expression (Max) observed for each gene.
- (E) t-SNE plots of wild-type SGNs with dot colors indicating subtype identity assigned by unsupervised graph-based clustering (left) and by Random Forest (right), a supervised clustering approach.
- (F) Scatterplot showing subtype identity of every cell predicted by unsupervised (x axis, "Graph-based") and supervised clustering (y axis, "Random Forest") methods. Only cells that had not been used for training the Random Forest classifier are shown. Cells that fall on the diagonal dotted line are the ones predicted correctly by the supervised method.
- (G) Subtype proportions among SGNs from three tonotopic regions predicted by each clustering method. Scale bar: 10  $\mu$ m (A).